Universität Hamburg
DER FORSCHUNG | DER LEHRE | DER BILDUNG

Searching for electron-positron pair cascades from GRB221009A

A thesis submitted in partial fulfillment of the requirements for the degree of
Master of Science

Lea Burmeister

Matriculation Number
6998139

First Supervisor
Prof. Dr. Dieter Horns

Date
May 19, 2024

Second Supervisor
Dr. Manuel Meyer

Faculty of Mathematics, Informatics and Natural Sciences
Department of Physics

Abstract

The Gamma Ray Burst (GRB) 221009A was detected with the LHAASO air shower array on October 9th 2022 with the highest photon energy at $13\,\text{TeV}$. The burst was also observed with *Fermi* Large Area Telescope (*Fermi*-LAT). Very high energy (VHE, energy E $\geq 100\,\text{GeV}$) γ rays interact with the extragalactic background light (EBL) and produce electron-positron pairs which are deflected by the intergalactic magnetic field (IGMF). They inverse Compton (IC) scatter with photons of the cosmic microwave background (CMB) to γ-ray energies, which in turn produce a cascade. These cascade photons are expected to arrive at the observer with a time delay and can be used to constrain the IGMF.

This Master's thesis simulates the cascade for various magnetic field strength of the IGMF between $B = 10^{-20}$ and $10^{-16}\,\text{G}$ using the CRPropa Monte Carlo code. These models were tested against data obtained with *Fermi*-LAT in various time bins after the burst. To compare the models with each other a log likelihood ratio test was performed. First, the time-resolved spectral energy distributions (SEDs) were derived. The GRB afterglow emission was assumed to originate from the cascade. The results showed that a model with the cascade at $B = 10^{-18}\,\text{G}$ is preferred. Then three different power law sources were added to the analysis to explain the astrophysical afterglow of the burst. It was shown that an afterglow source makes a difference to the results. Including the afterglow, magnetic fields below $10^{-17}\,\text{G}$ can be ruled out at $95\,\%$ confidence. Different models for the EBL were used and compared. It was shown that the choice of the EBL model is irrelevant for the results.

In further studies a model of the afterglow derived LHAASO observations should be used in the analysis. This would provide a better prediction of the afterglow emission and could make the results more rebust against the choice of the spectral index of the power law model.

Zusammenfassung

Der Gamma Ray Burst (GRB) 221009A wurde von LHAASO am 9. Oktober 2022 mit dem LHAASO-Luftschauer-Array mit der höchsten Photonenenergie bei $13\,\text{TeV}$ detektiert. Der Burst wurde auch von *Fermi*-LAT beobachtet. Gammastrahlen mit sehr hoher Energie (VHE) wechselwirken mit dem extragalaktischen Hintergrundlicht (EBL) und erzeugen Elektronen-Positronen-Paare, die durch das intergalaktische Magnetfeld (IGMF) abgelenkt werden. Sie streuen mit den Photonen der kosmische Mikrowellenhintergrundstrahlung (CMB), die wiederum eine Kaskade erzeugen. Es wird erwartet, dass diese Kaskadenphotonen den Beobachter mit einer Zeitverzögerung erreichen und zur Eingrenzung des IGMF verwendet werden können.

Diese Masterarbeit simuliert die Kaskade für verschiedene Magnetfeldstärken des IGMF zwischen $B = 10^{-20}$ und $10^{-16}\,\text{G}$ mit dem Monte-Carlo-Code CRPropa. Diese Modelle wurden anhand von Daten getestet, die mit *Fermi*-LAT in verschiedenen Zeitabschnitten nach dem Burst gewonnen wurden. Zum Vergleich der Modelle wurde ein Log-likelihood-Ratio-Test durchgeführt. Zunächst wurden die zeitaufgelösten spektralen Energieverteilungen (SEDs) erstellt. Es wurde angenommen, dass der GRB-Afterglow von der Kaskade ausgeht. Die Ergebnisse zeigten, dass ein Modell mit der Kaskade bei $B = 10^{-18}\,\text{G}$ bevorzugt wird. Dann wurden drei verschiedene Potenzgesetzquellen in die Analyse einbezogen, um den astrophysikalischen Afterglow des Bursts zu erklären. Es wurde gezeigt, dass der Afterglow einen Unterschied in den Ergebnissen macht. Durch die Einbeziehung des Afterglows konnten Magnetfelder unter $10^{-17}\,\text{G}$ mit $95\,\%$ Sicherheit ausgeschlossen werden. Es wurden verschiedene Modelle für das EBL verwendet und verglichen. Es wurde gezeigt, dass die Wahl des EBL-Modells für die Ergebnisse unerheblich ist.

In weiteren Studien sollte ein Modell des Afterglows, das aus den von LHAASO beobachteten Daten abgeleitet wurde, in die Analyse einbezogen werden. Dies würde eine bessere Vorhersage der Emission des Afterglows ermöglichen und könnte die Ergebnisse gegenüber der Wahl des Spektralindexes des Potenzgesetzes verlässlicher machen.

Content

Acknowledgements 49

CHAPTER 1

Introduction

Astroparticle physics is a relatively new field. It involves many subfields of physics: electrodynamics, mechanics, thermodynamics, nuclear physics, plasma physics, elementary particle physics and special and general relativity. Astroparticle physics was initially based on optical astronomy. Now elementary particles of astrophysical origin are studied.

In 1911–1912, for the first time Victor Hess measured a source of ionization radiation that becomes stronger with increasing altitude using balloons up to heights of $5\,km$ (Nobel Prize 1936). Also in 1912, Charles Thomson Rees Wilson developed the cloud chamber, with which it became possible to detect ionizing particles by virtue of the tracks they left in the detectors (Nobel Prize 1927). Since then, extraterrestrial cosmic radiation (Höhenstrahlung) has been of particular importance to the development of astroparticle physics.
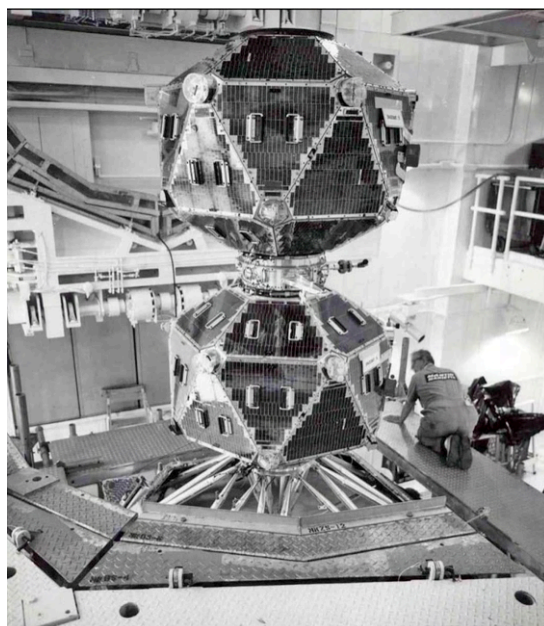

Figure 1.1: Vela satellites stacked for launch [1].

Otherwise, the observation of primary X rays and γ rays was impossible due to their absorption in the upper layers of the atmosphere. In the 60's and 70's the first X-ray (Uhuru 1970) and γ-ray satellites (Vela 1967, Figure 1.1) were launched. After that the first point sources were detected using high-energy astroparticles, e.g. Crab Nebula, Vela X1 and Cygnus X3.

In 1967 the first γ-ray bursts (GRBs) were discovered. They were detected by γ-ray detectors onboard of military reconnaissance satellites (Vela, Figure 1.1). The original purpose of these satellites was to check possible violation of the test-ban treaty on thermonuclear explosives. The discoveries were withheld until it became clear that the bursts came from outer space and not from the earth because of military secrecy. Since then, multiple X-ray and γ-ray satellites have been launched, including the *Fermi Gamma-ray Space Telescope (Fermi)* in 2008. Also earth-bound air-shower experiments and Cherenkov telescopes are able to observe other Very High Energy Sources (GeV-PeV) in the Milky Way and in extragalatic distances. The field of γ-ray astronomy is expanding rapidly.

Figure 1.2: Illustration of a GRB [2].

The Astronomy with charged particles on the other hand is more difficult. Irregular interstellar and intergalatic magnetic fields randomly alter the directions of charged particles [3]. Intergalatic magnetic fields (IGMFs) have not been detected so far and their strength is still unknown. The IGMF has been constrained using γ-ray observations and cosmology. Active Galactic Nuclei (AGN) and GRBs can be used to constrain the IGMF [4].

On October 9th 2022 the Large High Altitude Air Shower Observatory (LHAASO) detected GRB221009A with the highest photon energy at $13\,\mathrm{TeV}$. Over 140 photons between 3 and $13\,\mathrm{TeV}$ were detected. It was the most energetic and brightest GRB ever recorded, which is why it is called the "Brightest Of All Time" (the BOAT) [5], [6]. In this thesis this burst is used to search for signatures and thus to constrain the IGMF.

CHAPTER 2

Intergalactic Magnetic Field

Intergalatic magnetic fields (IGMFs) refers to the large-scale magnetic fields between clusters of galaxies. Their origin is still unknown. There are two types of scenarios for their origin. One approach is using Cosmological scenarios, for e.g. they come from primordial magnetic fields which have been produced either through decoupling transitions of fundamental forces, or by quantum fluctuations during the theorized inflationary period in the very early Universe. Another approach considers astrophysical scenarios. IGMFs could be produced from local effects in astrophysical objects, e.g. by ejection of magnetized plasma into intergalatic space by galaxies or AGN [4], [7].

IGMFs have not been detected so far. General constraints for the IGMF come from γ-ray observations and cosmology. Figure 2.1 shows an overview of the main constrains on the IGMF. An upper limit on the coherence length L_B comes from the size of the observable Universe. This is shown in Figure 2.1 as "Hubble horizon" in grey.

The IGMF decays due to magnetic diffusion. From the decay time one can derive a lower limit on L_B. In Figure 2.1 this is shown as "magnetic diffusion" in grey.

An upper limit on the field strength B can be derived from measuring the Zeeman splitting of H I lines. A larger IGMF would have impact on the observations. It is shown as "Zeeman effect" in grey in Figure 2.1.

Another constraint comes from mearuring the Faraday rotation of polarised radio emission from e.g. quasars. Faraday rotation is the rotation of the polarisation plane of polarised electromagnetic radiation travelling through a magnetic field. It is shown in red as "Faraday rotation" in Figure 2.1.

A theoretical approach is to consider a given mechanism of magnetic field generation and derive limits on the initial magnetic field. Then one can calculate the time evolution to the present day. The limit resulting from that is shown as "early magnetic dissipation" in blue in Figure 2.1.

Most of the observational limits come from observing the cosmic microwave background (CMB). Magnetic fields can impact background radiation in many ways. Assuming a homogeneous field one can derive the expected temperature anisotropies. This is shown in Figure 2.1 as "CMB

anisotropies" in green. Taking more effects, e.g. spectral distortion, into account one can im-
prove those upper limits (marked with "CMB spectrum" in yellow in Figure 2.1).

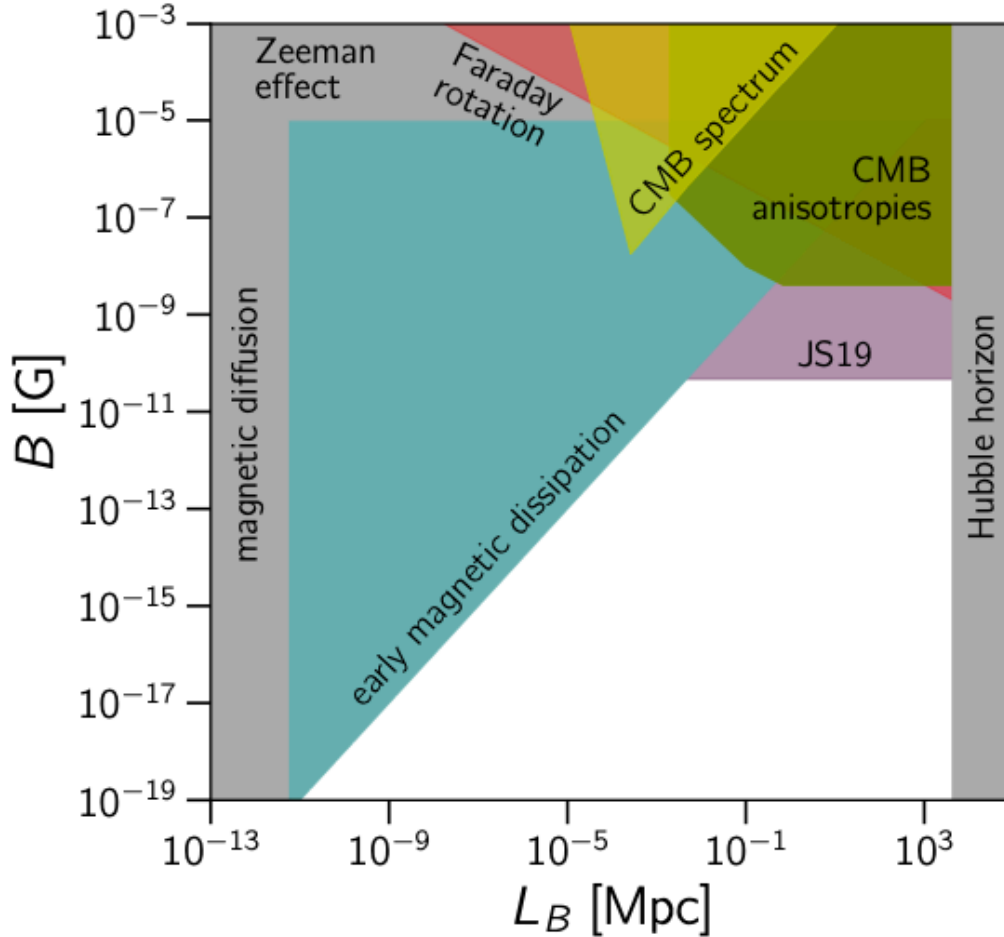Also shown in purple labelled "JS19" is the case of a scale-invariant spectrum [4].

Figure 2.1: Overview on the main constrains on IGMF [4]. Upper and lower bounds on L_B in grey ("magnetic diffusion" and "Hubble horizon"), upper limit in B in grey due to Zeeman splitting ("Zeeman effect"), constrain due to Faraday rotation in red ("Faraday rotation"), a limit due to an inital magnetic field in blue ("early magnetic dissipation"), constrains from CMB obervations in yellow and green ("CMB spectrum" and "CMB anisotropies") and the case of a scale-invariant spectrum in purple ("JS19").

2.1 Particle Cascades

γ-rays emitted by extragalatic sources (AGNs or GRBs) can be used to constrain the IGMF. At energies from $\sim$ 100 GeV to 100 TeV γ rays suffer photon-photon collision with the extragalactic background light (EBL, further explained in Section 2.1.1) and produce electron-positron pairs in particle pair production. The electrons and positrons get deflected by the IGMF. They scatter elastically off the CMB radiation, boosting their energy via inverse Compton (IC) effect. They produce a pair photon cascade. This process is illustrated in Figure 2.2. The cascade photons arrive at the observer with a time delay since they have to cross a larger distance than photons coming directly from the source.
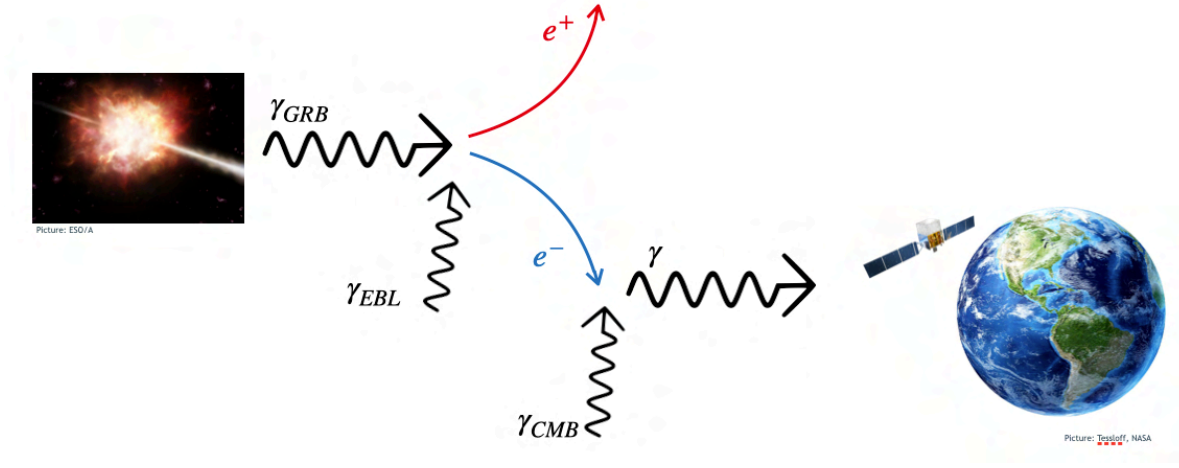
Figure 2.2: Illustration of the cascade production. GRB photons interact with the EBL and pair produce electron positron pairs which get deflected by the IGMF. They up-scatter CMB photons and produce a cascade.

To calculate the time delay it is assumed that the primary photon energy $E_p < 10\,\text{TeV}$ and the redshift $z \ll 1$. It is assumed that the electrons and positrons on average each have half of E_p. Then the average energy E_γ of the secondary photons is

$$E_\gamma = 0.8 \left(\frac{E_p}{\text{TeV}} \right)^2 \text{GeV}. \tag{2.1}$$

For a redshift $z \ll 1$ a secondary photon reaches the observer without another interaction. For $E_p < 10\,\text{TeV}$ E_γ is $< 10\,\text{GeV}$. The minimum energy E_e of an electron (or positron) that scatters a CMB photon is

$$E_e = 10.0 \left(\frac{E_\gamma}{\text{TeV}} \right)^{1/2} \text{TeV}. \tag{2.2}$$

The maximum flight path λ_{max} can be calculated with the energy-loss formula:

$$\left(\frac{dE}{E} \right)^2 = -k \, dx \tag{2.3}$$

with $k = \frac{4}{3}\sigma_T U/(mc^2)^2$, E the electron energy, σ_T the Thomson cross-section, U the energy density of the CMB radiation and m the electron rest mass. The total flight path λ_e is given by intergrating Equation (2.3) from the initial electron energy E_i from its production at position x_i to the final electron energy E_f at the position x_f where it scatters:

$$\lambda_e = (x_f - x_i) = \frac{1}{k} \left(\frac{1}{E_f} - \frac{1}{E_i} \right) < \frac{1}{kE_f} < \lambda_{max} = 0.04 \left(\frac{E_\gamma}{TeV} \right)^{-1/2} \text{Mpc}. \tag{2.4}$$

The upper limit of the magnetic deflection angle θ is given by

$$\theta < \frac{\lambda_{max}}{r_i} \tag{2.5}$$

with r_i the Larmor radius of a scattering electron with energy E_e (Equation (2.2)):

$$r_i = 10.0 \left(\frac{E_\gamma}{\text{TeV}}\right)^{1/2} \left(\frac{B}{10^{-18}\,\text{G}}\right)^{-1} \text{Gpc.} \tag{2.6}$$

Here B is the strength of the IGMF which is assumed to be coherent over the flight path. This leads to the time delay δt by the IGMF for a secondary photon with the energy E_γ (Equation (2.1)) from a source with distance x:

$$\delta t < \frac{\theta^2 x}{8c} = 2.4 \left(\frac{x}{\text{Gpc}}\right) \left(\frac{E_\gamma}{\text{TeV}}\right)^{-2} \left(\frac{B}{10^{-18}\,\text{G}}\right)^{2} \text{days.} \tag{2.7}$$

In observations the time delay will stay below δt because $\frac{1}{E_i} > 0$ and λ_{max} and r_i were calculated at the smallest possible electron energy. By performing observations at energies over $\sim 10\,\text{MeV}$ and on different time scales it is possible to search over a large range of IGMF strengths [7].

2.1.1 Extragalactic Background Light

The EBL is one of the fundamental observational quantities in cosmology. It includes the light from any truly diffuse background and the light from resolved and unresolved extragalactic sources. It is the emission between the wavelength of 0.1 and $1,000\,\mu$m. It can be called a repository of all energy released by nuclear and gravitational processes since the era of recombination. A big part of the radiation is shifted into the infrared (IR) wavelengths. This is due to absorption and reradiation by dust. The spectral shape and intensity contain information about the contents, formation and evolution of galaxies throughout cosmic history. They depend on many factors, e.g. the composition, size distribution and optical properties of the dust grain. There have been different approaches to model the intensity and spectral shape of the EBL at $z = 0$ thus to calculate the evolution of the comoving luminosity density with redshift [8]. The models used in this work are briefly discribed in this section.

Backward Evolution Models (BE)
For BE models one would first construct a library of galactic SEDs of galaxies in the local universe. Those galaxies should represent a range of observed galactic activities and morphologies. Then regress those over time. After that determine the evolution of the spectral luminosity density with redshift. The EBL is then obtained by an integration over the redshift [8]. A BE model used in this work is the model by Franceschini [9].

Forward Evolution Models (FE)

FE models are using the dependence of the redshift of the cosmic star formation rate (CSFR). First one determines the CSFR to then use the population synthesis models to calculate the spectral luminosity as a function of redshift. Afterwards the EBL is again obtained by an integration over the redshift [8]. In this work a FE model was used by Finke [10].

Semi-analytical Models (SA)

SA models use the formation and evolution of galaxies in a cold dark matter Lambda (ΛCDM) dominated universe. As initial conditions the cosmologial parameters from 5-year *Wilkinson Microwave Anisotropy Probe* (WMAP5) [11] observations are used. They follow the merger and growth of dark matter halos and emergence of galaxies which form when baryonic matter falls into the potential wells of the halos. Recent SA models are combined radiative transfer models with models for galaxy formation to determine the SEDs of galaxies [8]. An SA model that was used in this work is the model by Gilmore [12].

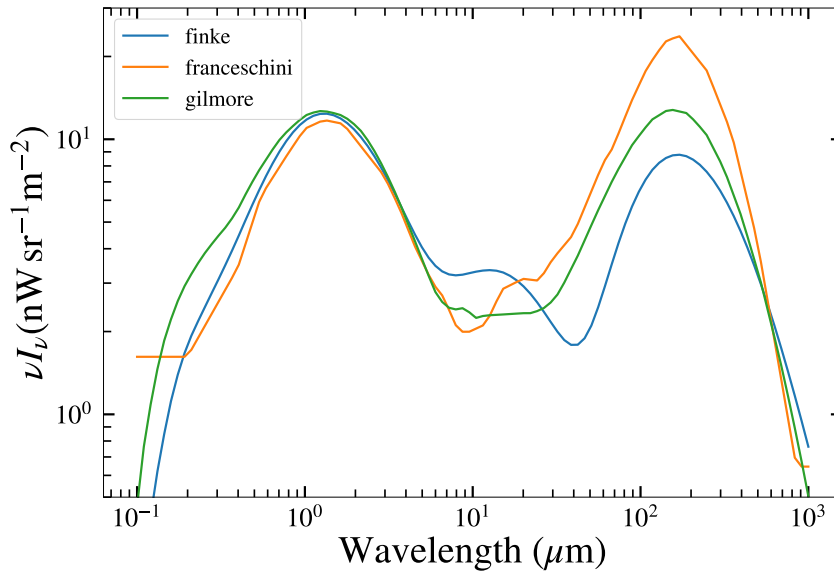The three models used in this work are all shown in Figure 2.3.

Figure 2.3: Calculated EBL intensity over wavelength for the used EBL models (provided by Sara Porras Bedmar). The Finke model is shown in blue, the Franceschini model in orange and the Gilmore model in green.

CHAPTER 3

Gamma Ray Bursts

GRBs are the most energetic explosions in the known Universe. They radiate between 10^{48} and 10^{55} ergs. They were discovered for the first time by the Vela satellites [13] in the late sixties by accident. GRBs are irregular pulses of γ-ray radiation which typically last less than a minute and have a non-thermal (broken power-law) spectrum. Their duration has two distinct peaks. The first one at approx. $0.3\,\text{s}$ and the second one at about $30\,\text{s}$ with a trough in between at approx. $2\,\text{s}$. The classification of GRBs is complicated but they can be divided into short-GRBs and long-GRBs. Short-GRBs last less than $2\,\text{s}$ while long-GRBs last more than $2\,\text{s}$.
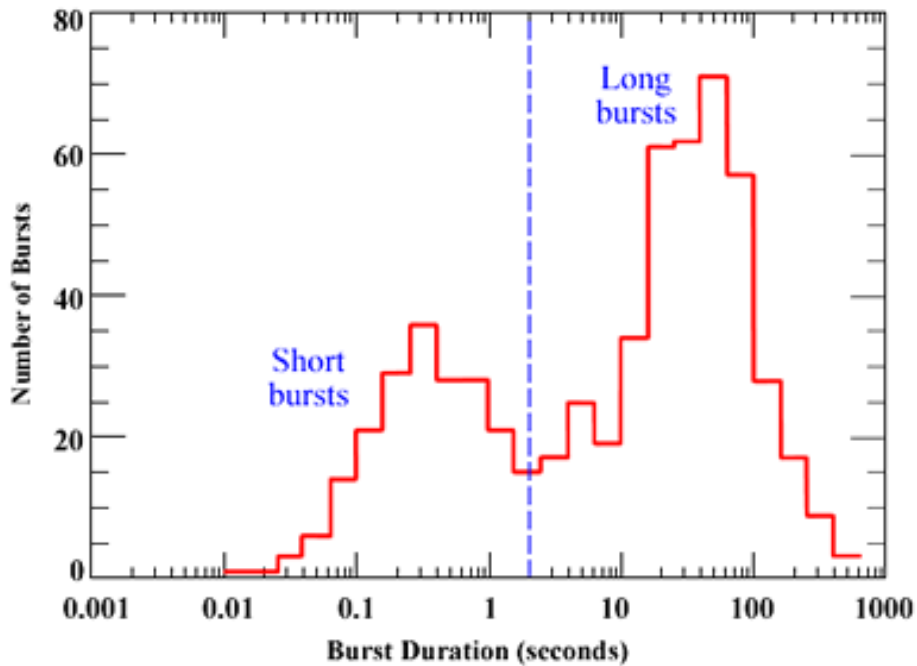

Figure 3.1: The number of bursts over the burst duration to show the difference between short and long GRBs (red histrogram). Short GRBs last less than $2\,\text{s}$ and long GRBs more than $2\,\text{s}$ (blue dashed line) [14].

Long-GRBs are one possible outcome of the collapse of massive stars. There has been observational evidence associating long-GRBs with core collapse SNa. They are typically found in star forming regions of galaxies. For several GRBs Type Ic supernovae have been detected spectroscopically associated with the GRBs.

Some short-GRBs might originate from mergers of compact objects in binary systems, e.g. two neutron stars or a neutron star and a black hole. A fraction of short-GRBs were observed in elliptical galaxies so they are associated with older stellar population. On average they are less energetic and at lower redshift. Those obervations are consistent with short-GRBs originating from neutron star mergers. But so far there is no proof of that theory. The connection of the classification between the duration and the physical origin of the bursts are more complicated and not fully understood. Figure 3.1 shows the number of short-GRBs and long-GRBs over burst duration to the difference.
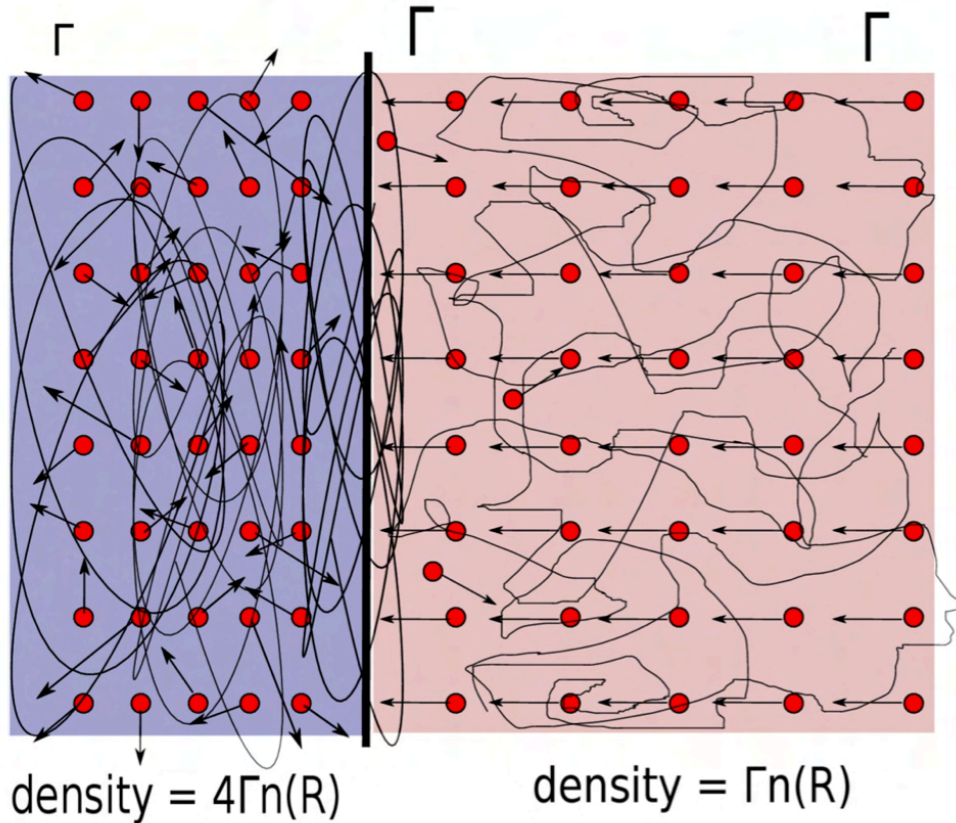

Figure 3.2: A schematic sketch of highly relativistic shock from the mean rest frame of the shocked fluid. On the right the unshocked medium. The cold, upstream particles stream towards the medium (black arrows) with Lorentz factor Γ. Black lines show the magnetic fields. The shocked medium on the left with Lorentz factor 4Γ, amplified magnetic fields and accelerated particles [15].

GRB outflows are highly relativistic. A relativistic shock theory was initially developed in context of AGN jets but also appears to be well suited for GRB outflows. The shock randomizes the orientation of the particle velocity vectors but does not change the Lorentz factor when crossing the shock front. In the comoving frame of the shocked fluid, the shocked fluid is travelling

with Lorentz factor Γ with respect to the unshocked fluid. The density of the unshocked fluid is Γn. Upstream particles then stream towards the shocked fluid with Lorentz factor Γ. The shock compresses the plasma by a factor 4 for highly relativistic shocks. It also amplifies magnetic fields and accelerates the particles. This is shown in Figure 3.2. Here one can see the upstream particles on the right side with stream towards the shocked plasma (left side). The arrows represent the particle velocity and the black lines show the magnetic fields.

One of the foremost unanswered questions about GRBs is regarding the physical mechanism by which prompt γ-rays are produced [15]. Synchroton radiation of electrons might play a huge role in the GRB prompt emission and afterglow. This theory is generally accepted. But depending on the exact physical conditions IC scattering could also play a role [16]. The brief prompt emission usually follows the afterglow. It is smoothly fading emission at longer wavelength, e.g. X-ray, optical or radio [15]. While the X-ray afterglow is present for almost all GRBs, only about $50\,\%$ show an optical and radio afterglow. Those are called dark GRBs [16]. The afterglow can be detectable for several days (X-ray) or several weeks or months (optical and radio) [15]. When X-rays scatter from unobservable dust layers that lie in the direction of the burst it results in bright rings. This is shown as an example for GRB221009A in Figure 3.3 [17].
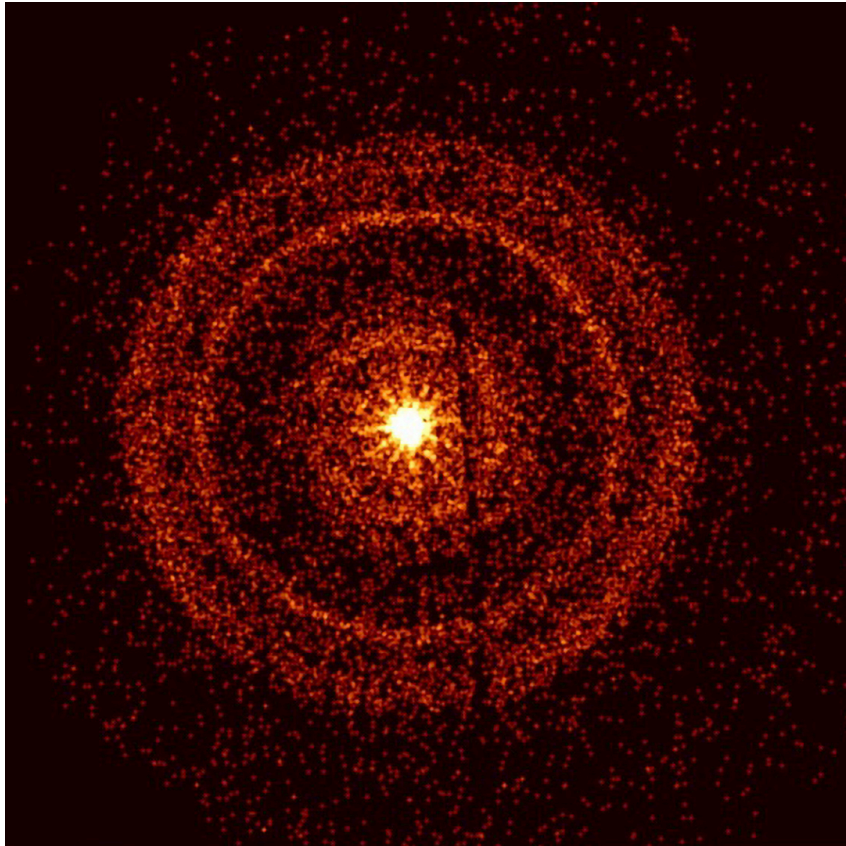

Figure 3.3: The afterglow of GRB221009A about an hour after it was first detected [17].

The understanding of GRBs has improved enormously in the last 15 years due to γ-ray and X-ray satellites and ground-based observatories [15].

3.1 GRB221009A

GRB221009A was detected on October 9 2022, at 13:16:59.99 Universal Time (UT) (T_0 in the following chapters) by the Gamma-Ray Burst Monitor (GBM) on the *Fermi* spacecraft [18]. At the same time it was also detected by *Fermi* Large Area Telescope (LAT) [19]. 53 minutes later the Burst Alert Telescope (BAT) on Neil Gehrels Swift Observatory (Swift) detected the burst. 143 s after the BAT trigger Swift's X-Ray Telescope (XRT) started observing [20]. The burst was also detected with the Large High Altitude Air Shower Observatory (LHAASO). LHAASO is a VHE gamma-ray extensive air shower detector to study cosmic rays and γ rays. LHAASO observed the burst for $6,000$ s before it moved out of its field of view [5]. It observed the GRB at its highest energy band [6]. The redshift of GRB221009A is $z = 0.151$. Its isotropic energy release $E_{\gamma,iso}$ is at $3 \cdot 10^{54}$ erg which is among the highest ever measured. LHAASO's Water Cherenkov Detector Array (WCDA) detected more than $64,000$ photons within the first $3,000$ s with an energy above 0.2 TeV (up to about 7 TeV).
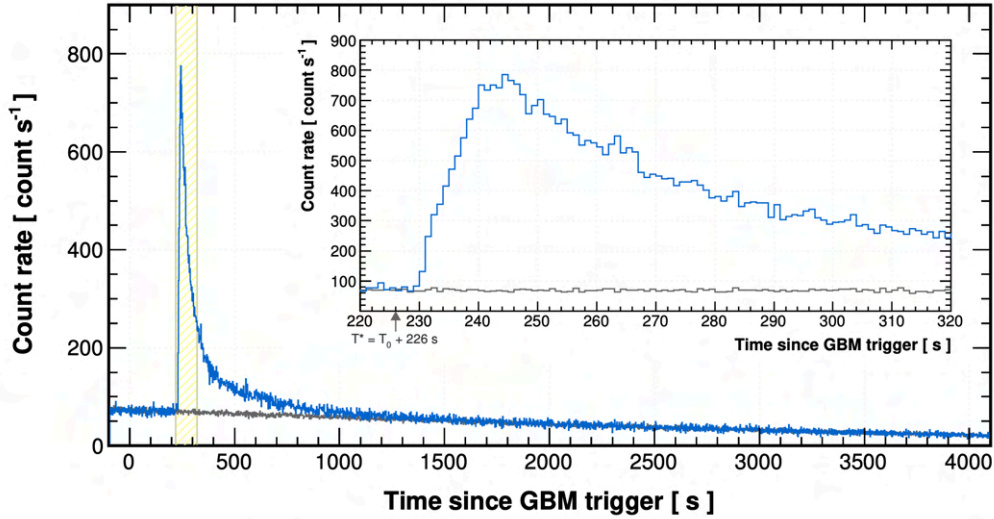

Figure 3.4: Lightcurve of GRB221009A observed by WCDA with a zoom-in on 220-320 s after T_0 (yellow shaded region) in the insert panel. The data is shown in blue and the estimated background in black [5].

The lightcurve of WCDA's observations are shown in Figure 3.4. The TeV photon flux began about 226 s after T_0 with the flux peak about 10 s later and a decay phase about 650s after the peak. Figure 3.5 shows the observed (B) and intrinsic (A) flux spectra for five time intervals in an energy range of ~ 200 GeV to ~ 7 TeV. Here, T^* refers to the start of the main burst ($T_0 + 226$ s). The observed spectra were fitted with a power law model with an exponential cutoff at 3.14 TeV and spectral indices between $2.7 < \Gamma < 3.1$ (see [5], Table S2). The intrinsic spectra were fitted with a power law model with spectral indices between $2.2 < \Gamma < 2.5$ (see [5], Table S2). This is consistent with the data with no evidence for a cutoff or spectral break [5]. The spectral models are further explained in Section 5.2.
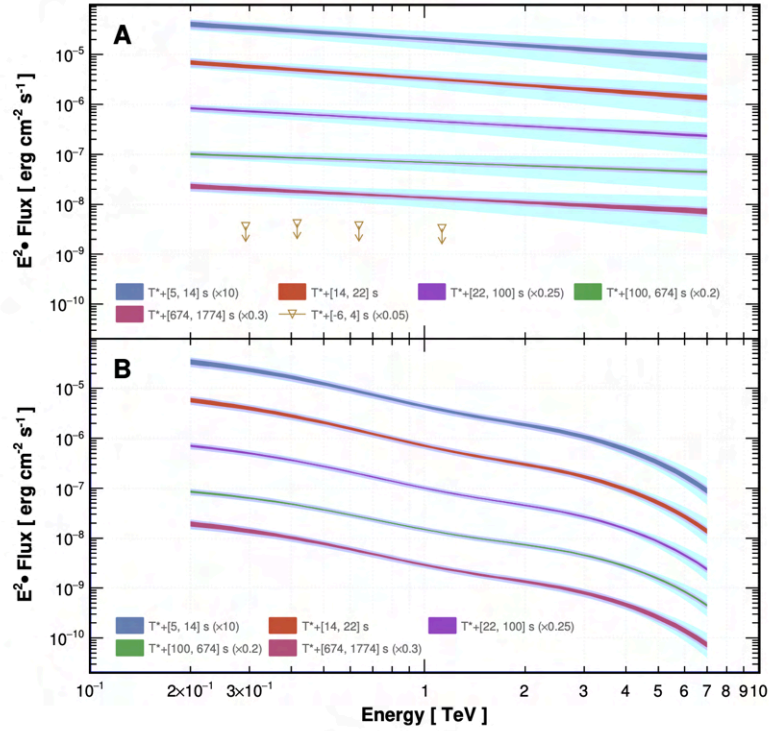
Figure 3.5: The intrinsic and observed spectra obtained with WCDA for five time-intervals. A: The intrinsic spectrum corrected for EBL attenuation with a power law model. B: the observed spectra obtained by reapplying the EBL attenuation to the corresponding intrinsic spectra. [5].

LHAASO's Kilometer Squared Array (KM2A) detected 142 γ-rays between 3 and 13 TeV within 230-900 s after T_0. The lightcurve is shown in Figure 3.6. The photon flux started at 230 s after T_0 with a peak at 245 s. The emission decreased after 300 s and faded out after 900 s [6].
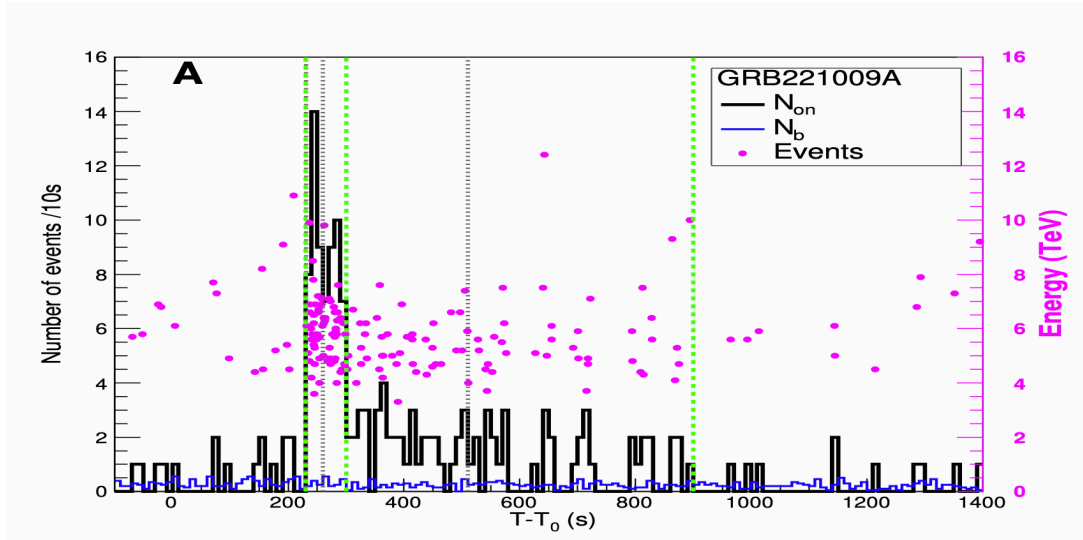
Figure 3.6: Lightcurve of GRB221009A observed by KM2A. The data of the burst is shown in black time bins of 10 s. The background is shown in blue. The green dashed lines are at 230, 300 and 900 s after T_0. The grey dashed lines indicates the peaks of the multi-pulsed emission observed by GECAM-C in the MeV band. The pink points show the energy and arrival time of each event [6].

Figure 3.7a shows the spectral energy distribution (SED) of the combined WCDA and KM2A

data for the two different time bins shown in Figure 3.6. The data was once fitted with a log parabola model (A) and with a power law model with exponential cutoff (B). As shown in [6], the power law model in favoured over the log parabola model. Figure 3.7b shows the intrinsic spectra for the same two time bins corrected for EBL absorption using the Saldana-Lopez model [21] fitted with a power law model with index $\Gamma = 2.35$ (first time bin) and $\Gamma = 2.26$ (second time bin, A). In panel B the intrinsic spectra using a re-scaled best-fit EBL model fitted with a power law model with index $\Gamma = 2.12$ (interval 1, red) and fitted with a log parabola (interval 2, blue) [6].
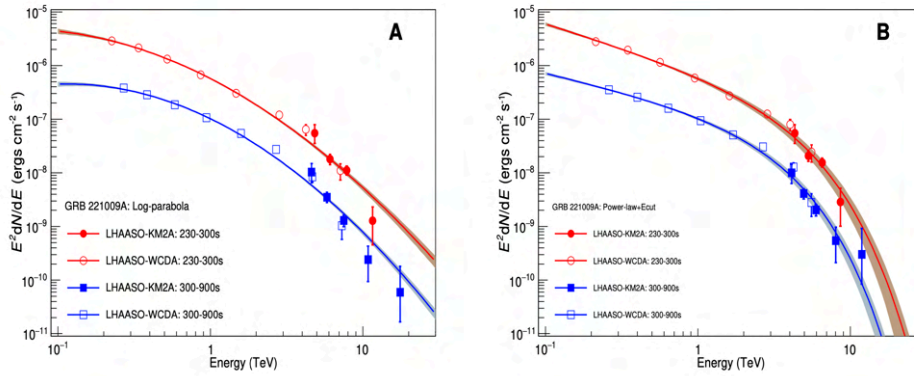
(a) The observed VHE spectra of the GRB by LHAASO for two time intervals. A: Data fitted with a log parabola model. B: Data fitted with power law model with exponential cut-off [6].
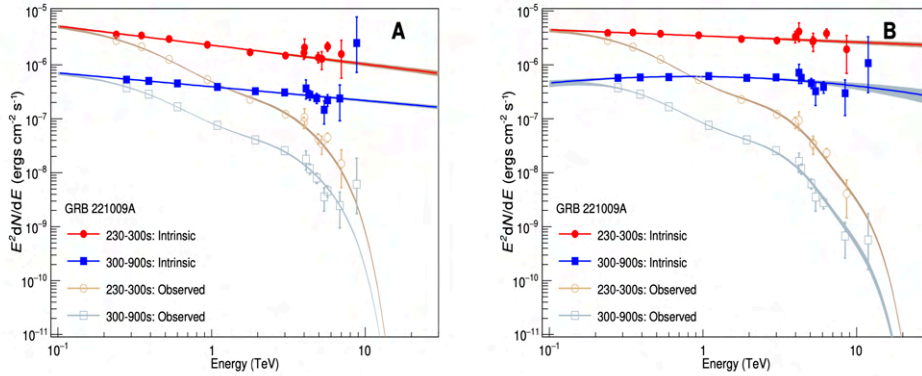
(b) The intrinsic VHE spectra of the GRB corrected for EBL absorption. A: Intrinsic spectrum corrected for EBL absorption using the model of Saldana-Lopez [21]. Data is fitted with a power law model. B: Intrinsic spectrum corrected for EBL absorption using the LHAASO-constrained EBL model. Interval 1 (red) is fitted with a power law model and interval 2 (blue) is fitted with a log parabola model [6].

Figure 3.7: The observed and intrinsic VHE spectra of GRB221009A by LHAASO [6].

In this work, the intrinsic spectrum of the LHAASO complete data set [6] was fitted with a log parabola model and used for the spectral shape of the cascade. This is further explained in Section 6.0.2.

GRBs provide a more accurate temporal information than e.g. blazars since they are not active over a longer time scale. This results in a more accurate limit for the IGMF since their VHE components depend strongly on the properties of the IGMF [4], [22]. The observed energy range

of the burst is higher than any previous observed GRB. Its large fluence saturated almost all γ-ray detectors [5]. Due to the high flux in the TeV energy band GRB221009A is very valuable opportunity to study the IGMF. Using the *Fermi*-LAT observations of the burst, constraints of the IGMF have already been derived [23], [24]. A lower bound was derived at $B = 10^{-19}$ G [24] and at $B = 10^{-18.5}$ G [23]. In these studies, a similar approach was used as in this work. To improve their results, this work uses more time bins in the analysis. This allows the derivation of a more precise model for the TeV emission of the LHAASO energy band and thus a more precise limit in the IGMF.

Fermi Large Area Telescope

The *Fermi Gamma-ray Space Telescope (Fermi)* was launched on June 11, 2008 by NASA and includes the Large Area Telescope (*Fermi*-LAT). The LAT measures directions, energies and arrival times of γ rays while rejecting background cosmic rays. One of its main focuses is to help understand the high-energy (HE) behaviour of GRBs and transients. It is a pair-conversion telescope with a converter-tracker, a calorimeter, an anticoincidence detector and a programmable trigger and data acquisition system. HE γ-rays interact by conversion into $e^+ e^-$ pairs. Fig. 4.1 shows an illustration of *Fermi*-LAT.
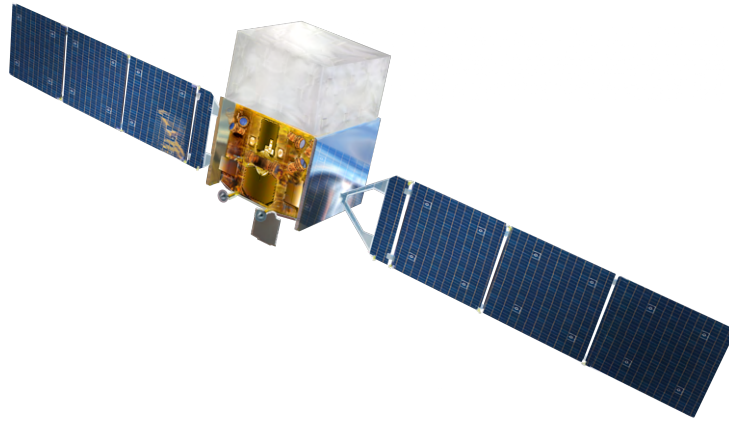
Figure 4.1: The *Fermi* Large Area Space Telescope [25].

Converter-tracker

The converter-tracker is the upper part of *Fermi*-LAT (Fig. 4.2). It consists of 18 x, y tracking planes each made of 2 layers of single-sided silicon strip detectors which are called the tracker-module. Here the passage of charged particles gets recorded and the tracks of particles resulting from pair production gets measured. This is used to reconstruct the direction of the incoming γ-rays. The 16 layers on top of the tracker are interleaved with high-Z material (Tungsten). Those are the converter planes of the converter-tracker. Here the γ-rays get converted into $e^+ e^-$ pairs.

Calorimeter

The calorimeter is the bottom part of *Fermi*-LAT (Fig. 4.2). Each module is made out of 96 CsI(Tl) crystals (2.7 x 2.0 x 32.6 cm). They are arranged horizontally in 8 layers of 12 crystals with a vertical depth of 8.6 radiation length. The layers are aligned by 90° with respect to their neighbour. At each end of every crystal is a photodiode to cover the full range of energy deposition due to electromagnetic showers from the $e^+ e^-$ pairs in the crystal. The energy can be measured from ~10 MeV up to 1 TeV. The second purpose of the calorimeter is to image the shower development profile to reconstruct the direction of the shower. Due to this, the calorimeter is also an important background discriminator.
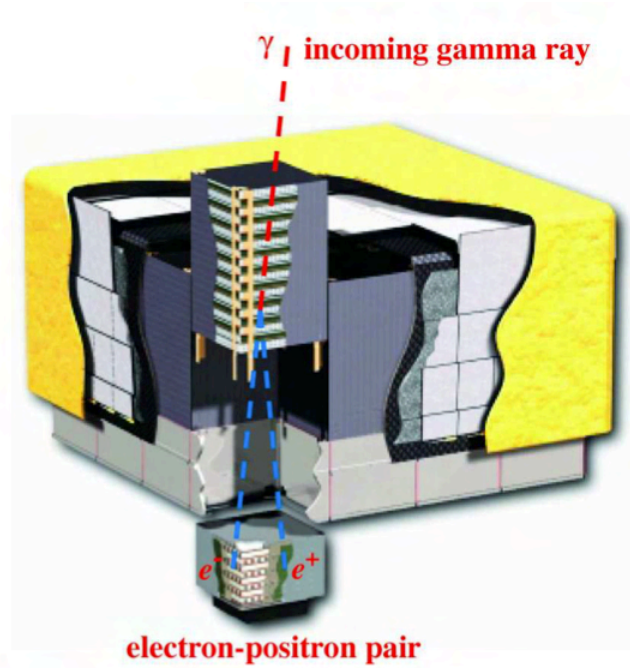
Figure 4.2: Schematic of *Fermi*-LAT with converter-tracker, calorimeter and anticoincidence detector [26].

Anticoincidence detector

The Anticoincidence detector (ACD) contains 89 plastic scintillator tiles. The scintillation light is collected by wavelength shifting (WLS) fibers within the scintillators. The WLS's are coupled to two photomultiplier tubes (PMTs) which are located around the bottom perimeter of the ACD. The ACD is surrounded by a low-mass micrometeorid shield to minimize the chance of light leaks. Its main purpose is to reject charged-particle background.

Data acquisition system

The data acquisition system (DAQ) implements a multi-level event trigger and collects the data from all other systems. It also provides an on-board science analysis platform and helps with on-board event processing [26].

CHAPTER 5

Analysis Methods

5.1 Maximum Likelihood Analysis

To analyse Fermi-LAT data, a likelihood, $\mathcal{L}$, applicable to the data is constructed and used to find the best fit model parameters. $\mathcal{L}$ is the probability of obtaining data given an input model. For LAT that input model is the distribution of γ-ray sources in the sky.

The LAT data will be binned into many bins in sky position and energy containing a small number of counts. The counts in each bin are characterized by the Poisson distribution. $\mathcal{L}$ is described by the product of probabilities of observing detected counts in each bin. The probability p_i of detecting n_i counts in the i-th bin is

$$p_i = m_i^{n_i} \frac{e^{-m_i}}{n_i!}, \tag{5.1}$$

with m_i the number of counts in the i-th bin. Since $\mathcal{L}$ is a product of all the p_i's it can be written as

$$\mathcal{L} = \prod_i m_i^{n_i} \frac{e^{-m_i}}{n_i!}. \tag{5.2}$$

Then $\prod_i e^{-m_i}$ is the same as $e^{-\sum_i m_i}$. Also $\sum_i m_i$ is N_{exp} which is the total number of predicted counts from a given model. Taking that into account, $\mathcal{L}$ becomes

$$\mathcal{L} = e^{-N_{exp}} \prod_i \frac{m_i^{n_i}}{n_i!}. \tag{5.3}$$

Equation (5.3) is called the binned likelihood. It has finite size bins and n_i that may be either greater than 1 or 0. But binning destroys information and accuracy. If the bin size gets infinitesimal than n_i would either be 0 (no counts) or 1 (detected count). Then $\mathcal{L}$ looks like

$$\mathcal{L} = e^{-N_{exp}} \prod_i m_i, \tag{5.4}$$

which is called the unbinned likelihood. This is more accurate but the large number of counts increases computation time to calculate. That is why usually the binned likelihood (Eq. (5.3)) is used [27]. Often the log likelihood is used:

$$\ln \mathcal{L} = \sum_i \ln \frac{m_i^{n_i}}{n_i!} - N_{exp}. \tag{5.5}$$

The loglikelihood ratio is a way to compare two statistical models to check if a hypothesis is preferred over another. In this work various values for strength B of the IGMF were tested. With variing B, the number of expected counts m_i changes since m_i is a function of the source model. The likelihood ratio is given by

$$\lambda(B) = \frac{\mathcal{L}(B)}{\mathcal{L}(\hat{B})}, \tag{5.6}$$

where $\hat{B}$ is the magnetic field strength that maximizes $\mathcal{L}$. The log likelihood ratio has the form of

$$-2 \ln \lambda(B) = -2 \cdot (\ln \mathcal{L}(B) - \ln \mathcal{L}(\hat{B})). \tag{5.7}$$

Equation (5.7) has an approximate χ^2 distribution with 1 degree of freedom. In this work a one-sided 95% confidence interval is used. That corresponds to Equation (5.7) equals to 2.71 [28], [29]. In this study, the log likelihood values were derived for multiple time bins and then summed up over time before the log likelihood ratio was calculated. This is further explained in Chapter 6.

5.2 Spectral Models

The spectral models used in this work are described in this Section. A model often used to describe the spectral shape of γ-ray point sources is the power law given by:

$$\frac{dN}{dE} = N_0 \left(\frac{E}{E_0} \right)^{-\Gamma}, \tag{5.8}$$

where N_0 is the normalization, Γ the spectral index and E_0 is the reference energy chosen as the energy where the error on the absolute flux is minimum. Another common model is the log parabola,

$$\frac{dN}{dE} = N_0 \left(\frac{E}{E_0} \right)^{-(\alpha + \beta \ln (E/E_0))}, \tag{5.9}$$

with N_0 and α as the flux and spectral index. β gives the curvature of the spectrum.
To both models an exponential cutoff $e^{-E/E_{cut}}$ can be added,

$$\frac{dN}{dE} = N_0 \left(\frac{E}{E_0} \right)^{-\Gamma} e^{-E/E_{cut}}, \tag{5.10}$$

$$\frac{dN}{dE} = N_0 \left(\frac{E}{E_0}\right)^{-(\alpha + \beta \ln(E/E_0))} e^{-E/E_{cut}}. \tag{5.11}$$

The usual way to describe the spectrum of a source is the spectral energy distribution (SED),

$$S(E) = E^2 \left(\frac{dN}{dE}\right). \tag{5.12}$$

which describes the spectrum multiplied with E^2 [30].

In this work, the spectrum of GRB221009A is assumed to be a log parabola with an exponential cutoff due to the data from [6]. This is further explained in Chapter 6.

5.3 *fermipy* Package

The LAT data is publicly available provided by the Fermi Science Support Center (FSSC)[1]. The FSSC also supports public software tools to analyse LAT data. Fermi *ScienceTools* is written in C++ with a python interface (`pyLikelihood`). *Fermipy* is a python software package based on the *ScienceTools*. It also relies on other open-source python libraries like *NumPy*, *Scipy* or *Astropy*.

The global analysis object is `GTAnalysis`. It manages the data and model preparation and provides the analysis methods. It uses a configuration file in the YAML format. In there, the analysis parameters like the data selection, the region-of-interest (ROI) and the model specification are present. For the model all sources within a chosen square region are selected to be included in the model. Also the galactic and isotropic background are added to the model. In this work, cascade predictions simulated with CRPropa for GRB221009A are used for the model.

The method `setup` runs the data and model preparation by executing appropriate *gt-tools*: `gtselect` for data selection, `gtmktime` for data filtering, `gtbin` for data binning, `gtltcube` for livetime calculation, `gtexpcube2` for exposure calculation and `gtsrcmodel` for calculation of spatial templates for individual model components.

The method `optimize` finds the best fit values for the spectral parameters of all components of the model [31].

With `free_sources` parameters of the model can be freed [32]. In this work, all parameters of the isotropic background and the normalization parameters of the galactic background have been freed. While setting up the data and model preperations, a test statistic (TS) is generated at each point in the ROI, which is given by:

$$\text{TS} = -2 \cdot (\ln \mathcal{L}_0 - \ln \mathcal{L}_1). \tag{5.13}$$

Here, a log likelihood ratio was calculated to compare the model without any additional source present ($\mathcal{L}_0$) to the model with an additional source ($\mathcal{L}_1$) [27], [32]. In this study, the normal-

---

[1]URL: https://fermi.gsfc.nasa.gov/ssc/

ization parameters of all sources with TS < 4 are freed. In addition, all shape parameters of all sources within a square area of $3° \times 3°$ and all normalization parameters within $10° \times 10°$ (both centered on the location of GRB221009A) are freed. The cascade component is fixed.

The `fit` method performs a likelihood fit for all free parameters of the model [32].

`sed` extracts the spectral energy distribution (SED) of the source. It resturns a dictionary with the characteristics in each energy bin (flux, flux errors, flux upper limits, TS, predicted counts). The SED is computed by replacing the spectral model of the source with a powerlaw and performing a fit of the normalization in each energy bin. It also can generate plots of the measured flux in each bin and the best-fit global parameterization of the source. Also the profile likelihood versus the source flux is extracted in each energy bin. An example of a generated plot for GRB221009A is shown in Figure 5.1 [31].
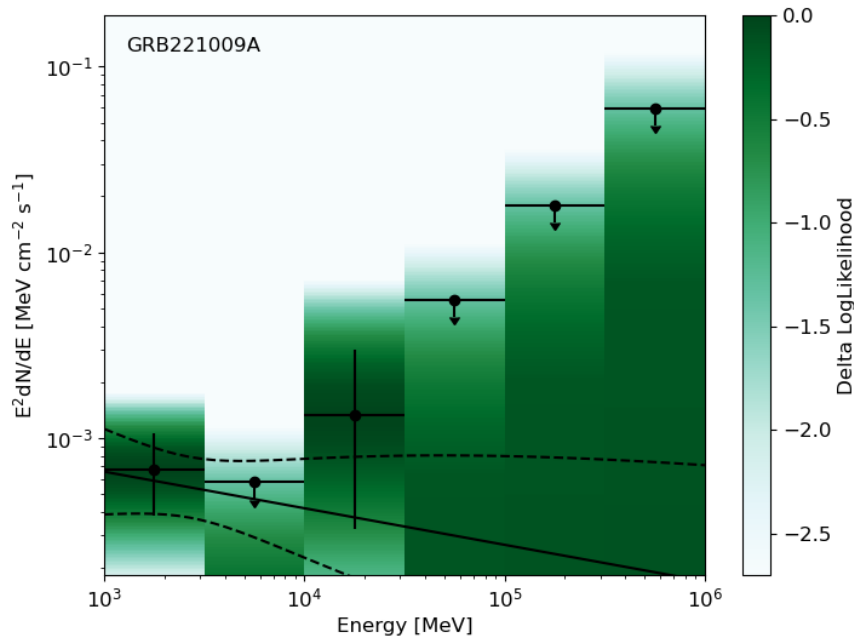
Figure 5.1: SED of GRB221009A in the third time bin (see Table 6.1) from 1 GeV to 1 TeV generated by `sed`. The flux points and upper limits are shown in black. The computed SED is shown as a black (dashed) lines. The log likelihood ratio values as a function of energy fluxes are shown in green in each energy bin.

`tsmap` generates a map of the $\sqrt{TS}$ value (Eq. (5.13)) at each spatial bin in the ROI [32]. At the end, the method `write_roi` writes all the results in an output file [31].

5.4 CRPropa 3.2

CRPropa 3.2 is a Monte Carlo code used to simulate the propagation of high-energy particles in the Universe. CRPRopa was developed in the early 2000s as a numerical cosmic ray transport code. It was one of the first propagation codes to perform transport of ultra-high-energy cosmic rays (UHECR) across the intergalactic space. It enabled simulations of three-dimensional

trajectories including deflections by magnetic fields and of one-dimensional propagation along straight lines [33].

The basic concept of CRPropa is to split up everything into independent modules. Those can be used in any combination and do not require each other to operate. During the propagation CR-Propa is repeatedly looping a cosmic ray through a list of active modules until a module signals the propagation as finished [34].

Since the first version CRPropa has been significantly improved. It is now possible to perform propagation of electromagnetic cascades in the intergalactic medium very efficiently. In previous versions the propagation was performed separately by the stand-alone cascading codes EleCa [35] and DINT [36]. Interaction modules were implemented for dominant electron and photon processes (e.g. `EMPairProduction` and `EMInverseComptonScattering` for pair production and IC scattering). The modules are based on EleCa code. They have been successfully used in number of works including Fermi-LAT contraints on IGMF [33].

In this work CRPropa 3.2 is also used to generate the electromagnetic cascade of GRB221009A. The simulations are performed in the large sphere observer framework. The source is at the origin of the sphere. The radius is equal to the comoving distance D to the source. All relevant particle interactions are included, meaning energy losses through pair production, IC scattering, synchroton emission of electrons in an expanding universe. The time delay of the cascade photons is calculated through

$$\tau \approx c^{-1}(d - D), \qquad (5.14)$$

with c the speed of light and d the propagation length. From the simulations, one receives a multidimensional histogram of photon counts $\mathcal{N}$. This histogram can be converted into the number of counts arriving per injected energy ϵ, observed energy E, solid angle Ω, time delay interval $d\tau$, and injected particle in the interval $\Delta\epsilon$:

$$\frac{d\mathcal{N}}{d\epsilon dE d\Omega} = \frac{1}{N_{inj}(\Delta\epsilon)} \frac{\mathcal{N}}{\Delta\epsilon \Delta E \Delta\tau \Delta\Omega}, \qquad (5.15)$$

with N_{inj} the number of injected particles and ΔE, $\Delta\tau$ and $\Delta\Omega$ the chosen bin width of the histogram for each quantity. This initial cascade spectrum can be convolved with the injected spectrum and integrated over the delay times to obtain the cascade flux that arrives within a maximum time delay τ_{max} for an arbitrary injected (time-averaged) photon spectrum $dN/d\epsilon$:

$$\frac{d\mathcal{N}}{dE d\Omega} = \int\limits_0^\infty d\epsilon \int\limits_0^\infty d\epsilon' \frac{dN}{d\epsilon'} \int\limits_0^{\tau_{max}} d\tau \frac{d\mathcal{N}}{d\epsilon' dE d\tau d\Omega} \approx \sum_i \sum_j \Delta\epsilon_i \Delta\tau_j w_i \left(\frac{d\mathcal{N}}{d\epsilon dE d\tau d\Omega} \right)_{ij}, \qquad (5.16)$$

with the spectral weights $w_i = \int_{\Delta\epsilon_i} \frac{dN}{d\epsilon} d\epsilon$ for the i-th energy bin of the injected spectrum $\Delta\epsilon_i$ [22]. The model specifications are contained in a configuration file in the YAML format. The specifications used in this work are further explained in Section 6.0.2 and an example of the configuration file is shown in Section A.1 (Figures A.2 and A.3).

CHAPTER 6

Results

This chapter shows the results of using the γ-ray observations from GRB221009A to constrain the IGMF. First the cascade was simulated using CRPropa 3.2 (see Sections 5.4 and 6.0.2). This was then used for the analysis with *fermipy* (see Sections 5.3 and 6.0.1). Then the log likelihood ratio was calculated (see Equation (5.7)). Section 6.2 compares the results using different models for the EBL. In Section 6.3, the astrophysical afterglow is included.

As explained in Section 2.1 cascade photons are expected to arrive at the observer with a time delay. Figure 6.1 shows an example of the predicted time delay assuming a strength of 10^{-17} G for the IGMF in a chosen time window of 0-$20,000$ s. The time delay was calculated by CRPropa using Eq. (5.14). In blue one can see all photons coming from the GRB. The cascade photons are shown in orange and primary photons in green. This shows that the cascade photons arrive with a time delay of at least up to $20,000$ s. One can see that more photons arrive with a shorter time delay and the number of photons decreases with increasing time delay. For a fixed distance of the source and a fixed magnetic field strength, the time delay only depends on the energy of the cascade photons (see Equation (2.7)). As mentioned in Section 3.1, the burst was detected with a high flux in the TeV energy band (see also Figure 3.6). So many of these photons should arrive with a shorter time delay and less with increasing time delay. One can also see that the simulations predict a time delay up to $5,000$ s for the primary photons. Primary photons do not arrive with a time delay. Using CRPropa, the time resolution of the simulation depends on the redshift of a source and the minimum step size. GRB221009A is at redshift $z = 0.15$. The chosen minimum step size for the simulation was 10^{-6} pc which corrensponds to a time resolution of 2 min. Due to the time resolution, the simulation can't distinguish between primary and cascade photons within the first $6,000$ s. The reason is a priori not known. Because of that, it makes sense to choose an observation window after the GRB and exclude times where the time resolution of the simulation suffices to distinguish between the primary and secondary components.
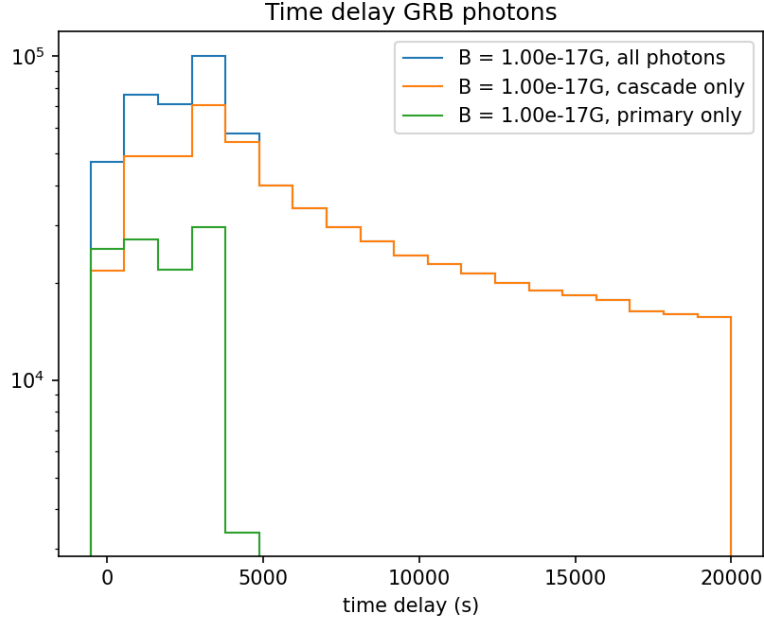
Figure 6.1: Approx. time delay of GRB photons for a strength of $B = 10^{-17}$ G for the IGMF. All photons coming from the burst are shown in blue, cascade photons in orange and primary photons in green.

Within the *Fermi*-LAT collaboration the complete data detected from GRB221009A with *Fermi*-LAT was analysed [37]. Figure 6.2 shows the late emission observed by *Fermi*. Here the data was divided into several time bins (blue and red crosses show the fluxes between different energy ranges in the bottom panel).
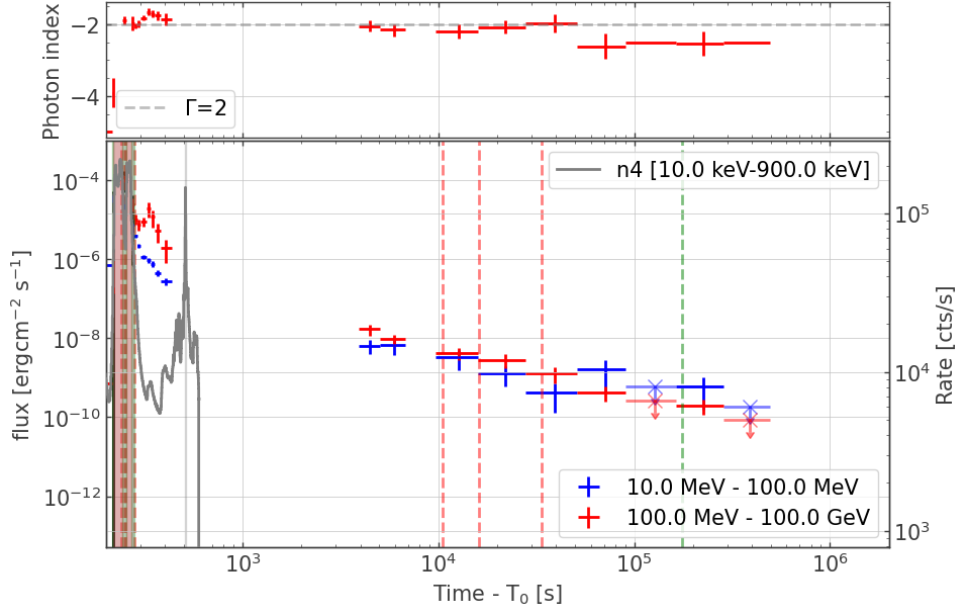
Figure 6.2: Late time emission of GRB221009A observed by *Fermi*-LAT. The top panel shows the photon index. The bottom panel shows the rate of events in the GBM detector n4 in grey, the flux between $10\,\text{MeV}$ and $100\,\text{MeV}$ in blue and the flux between $100\,\text{MeV}$ and $100\,\text{GeV}$ in red. The red dashed lines correspond to arrival times of the $>10\,\text{GeV}$ photons. The green dashed line is the arrival time of the last event with probability >0.9 to be associated with GRB221009A [37].

To be consistent with that in this work, the same time bins were chosen for the simulations and

the analysis. Since the cascade photons arrive with a time delay only the 9 latest time bins from Figure 6.2 were used and two more time later bins of 2 weeks and 5 months were added. The exact time bins are shown in Table 6.1. Here T_0 refers to the time where the first detector on-board *Fermi* was triggered on GRB221009A. First, time bins within the first $6,000\,$s have been included in the analysis (time bins Nr. 1 and 2) to see their impact on the results. They have been removed again later (see Section 6.3).

Table 6.1: Chosen time bins for the simulations and analysis [37].

Time bin Nr.	$T_{start} - T_0$	$T_{stop} - T_0$
1	$3,920\,$s	$5,010\,$s
2	$5,010\,$s	$6,810\,$s
3	$9,630\,$s	$15,870\,$s
4	$15,780\,$s	$27,810\,$s
5	$27,810\,$s	$51,090\,$s
6	$51,090\,$s	$90,570\,$s
7	$90,570\,$s	$164,130\,$s
8	$164,130\,$s	$284,490\,$s
9	$3.3\,$d	$18.3\,$d
10	$18.3\,$d	$33.3\,$d
11	$33.3\,$d	$183.3\,$d

A cascade is expected to be in an energy range above $\sim 10\,$MeV. That is why for the analysis an energy range from $100\,$MeV to $1\,$TeV was chosen.

6.0.1 *Fermi*-LAT Analysis with *fermipy*

For the analysis, all sources within a region of $15° \times 15°$ were selected for inclusion in the model (centered on the location of GRB221009A). But only data within a $10° \times 10°$ region of interest (ROI) were considered for the analysis. The isotropic and galactic background also have been added to the model. The spectral template `iso_P8R3_SOURCE_V3_v1.txt` has been used for the isotropic background. For the galactic background, the spectral and spatial template `gll_iem_v07.fits`[2] was used. The cascade predictions simulated with CRPropa were then used as a model for the GRB in the analysis with *fermipy* (see Section 5.3). The cascade was modelled as a point source and not as an extended source because the size of the halo is smaller than the point spread function (PSF) of *Fermi*-LAT for the low magnetic fields tested in this work. The analysis was performed using *gt-tools*. With the method `fit` the log likelihood value was derived. The analysis was repeated for all time bins shown in Table 6.1. The log likelihood values were summed up over time. This has been done for each tested magnetic field. Then the log likelihood ratio was calculated (see Equation (5.7)). The parameter choices for the analysis are shown in Table 6.2. A time range of 6 months divided into the time bins from Table 6.1 and

---

[2]URL: https://fermi.gsfc.nasa.gov/ssc/data/access/lat/BackgroundModels.html

an energy range from $100\,\mathrm{MeV}$ to $1\,\mathrm{TeV}$ as mentioned above were chosen. The instrument response function `P8R3_SOURCE_V3` was used. This class is usually used for the analysis of point sources [27]. A maximum zenith angle of $90°$ was used to reduce the contamination from the γ-rays Earth limb produced from the interaction of the cosmic rays with the upper atmosphere. An example of a configuration file in which all settings are defined for the analysis can be found in Section A.1 (Figure A.1).

Table 6.2: Parameters for the analysis using *fermipy*.

Parameter	Selection
Time Range	6 months
Energy Range	>100 MeV
ROI size	10° x 10°
Max. Zenith Angle	90°
Filter	DATA_QUAL>0 && LAT_CONFIG==1
Spatial binning	0.1° / pixel
Energy binning	8 bins per decade
Event Class / IRFs	P8R3_SOURCE_V3

The agreement of the data and model can be estimated by calculating the TS as described briefly in Section 5.3. Figure 6.3 shows the $\sqrt{\mathrm{TS}}$ map for the 11th time bin (see Table 6.1) with using the cascade predictions for a magentic field strength of 10^{-16} G for the IGMF. Low values are shown in black and the highest values in yellow. Here one can see only a few spots in the outer part of the diagram, where $3\sigma > \sqrt{\mathrm{TS}} > 0$. That shows that the model fits the data very well and all relevant sources are described by the model.
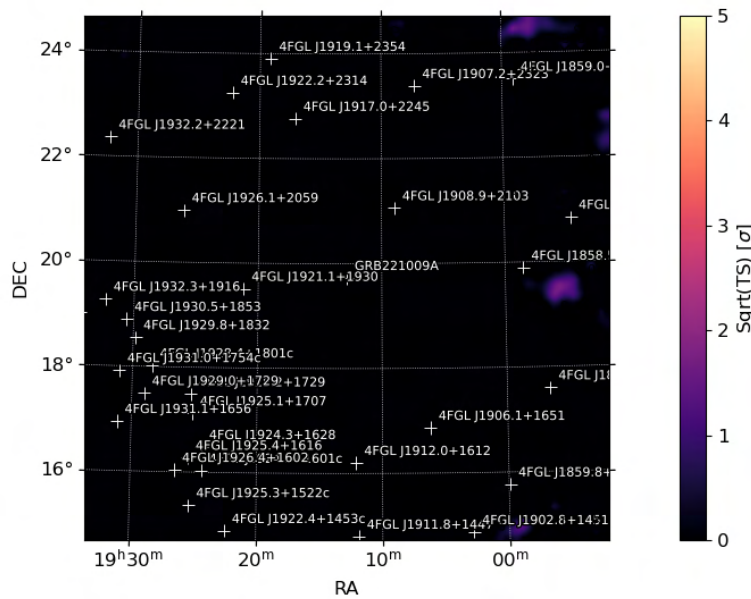

Figure 6.3: $\sqrt{\mathrm{TS}}$ map for a strength of $B = 10^{-16}$ G for the IGMF for the 11th time bin (see Table 6.1). The $\sqrt{\mathrm{TS}}$ values are shown in different colours with the lowest value in black diverging into pink, red and yellow for increasing values.

In preperation the log likelihood values were also derived using the `sed` method in *fermipy*. It was shown that this method is more constraining than using the `fit` method. So it was assumed that it is less accurate. So in the following results only the `fit` method is used. One can find a detailed explaination of the `sed` method and a comparsion in Section A.2.

6.0.2 Cascade Modelling with CRPropa

For the simulations, standard ΛCDM cosmology with $H_0 = 70 \, \mathrm{km \, s^{-1} \, Mpc^{-1}}$ and a matter density of $\Omega_m = 0.3$ was used (default values of CRPropa). Monochromatic γ rays were injected into a cone with opening angle $\theta_{jet} = 1.6°$ from the source with the central axis pointing along the negative x-axis in the simulation coordinate system. The energies ϵ were equal to the central energies of bins $\Delta\epsilon$ between $1 \, \mathrm{GeV}$ and $\approx 31.6 \, \mathrm{TeV}$. The tolerance parameter, which determines the numerical precision, was set to 10^{-16}. As mentioned before, the chosen minimum step size was $10^{-6} \, \mathrm{pc}$ which corrensponds to a time resolution of $2 \, \mathrm{min}$. Particles were stoped tracing eather if their energy droped below $0.1 \, \mathrm{GeV}$ or their total propagation distance became larger than $\approx 0.62 \, \mathrm{Gpc}$ to reduce computational time. The number of injected particles was set to 100 (40 for $B = 10^{-16} \, \mathrm{G}$ to reduce computational time) in a single simulation. 40 (99 for $B = 10^{-16} \, \mathrm{G}$) independent simulations were performed and than combined into a single spectrum. The cascade was simulated with CRPropa for different strengths for the IGMF. Turbulent magnetic fields between $10^{-20} \, \mathrm{G}$ and $10^{-16} \, \mathrm{G}$ were tested in logarithmic steps of 0.5. A configuration file in which all settings are defined can be found in Section A.1 (Figures A.2 and A.3). For the spectral shape of the cascade, the intrinsic spectrum from the LHAASO complete dataset [6] was fitted with a log parabola. This is shown in Figure 6.4.
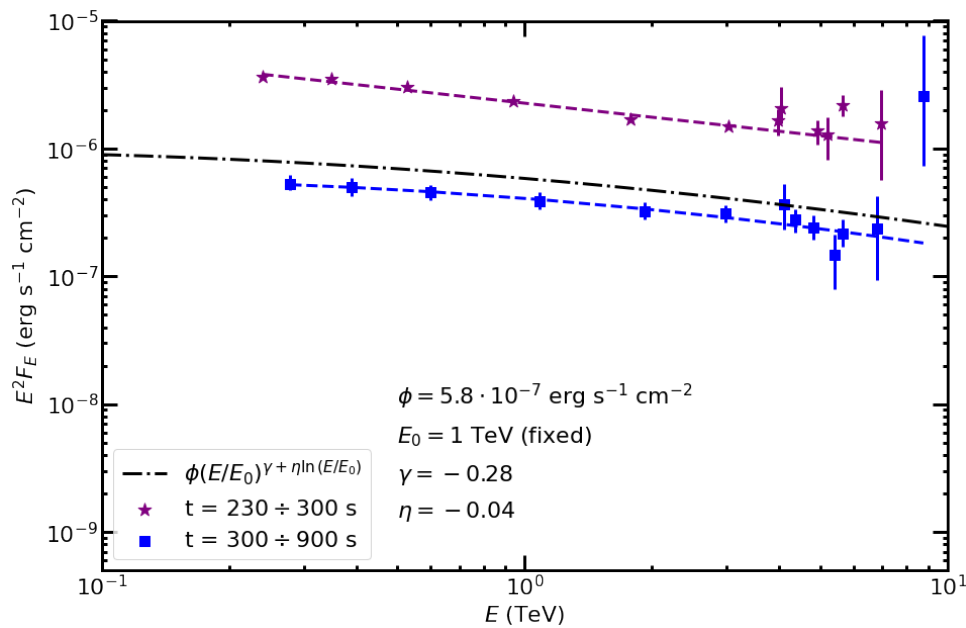

Figure 6.4: Intrinsic VHE spectrum from [6]. The spectrum from 230-300 s after T_0 is shown in purple and the spectrum between 300 and 900 s in blue. The black dashed line corresponds to the fit with a Log Parabola (provided by Francesco G. Saturni, in preperation).

In purple and blue there are the points from two different time intervals (see Section 3.1 and Figure 3.6). The black dashed line represents the fit with a log parabola with temporal weighting over the bin duration. The parameters from that fit were than used for the simulation with an exponential cutoff at 13 TeV because that was the highest photon energy detected by LHAASO [6] (see Section 3.1). The exact parameters are shown in Table 6.3.

Table 6.3: Parameters for the spectral shape of the cascade used for the simulations.

Parameter	Selection
Prefactor	$3.62 \cdot 10^{-19} \frac{1}{(cm^2\, eV\, s)}$
Scale	10^{12} eV
Index	2.28
Curvature	0.04
Cutoff	$1.3 \cdot 10^{13}$ eV

6.1 Time resolved Spectral Energy Distributions

The method `sed` extracts the SED of a source (see Section 5.3). Figures 6.5,6.6 show the measured flux for each used time bin generated by `sed` during the analysis in blue. Every detection with TS > 2 is considered a data point, everything is considered a upper limit. In Figure 6.5c a data point with a very large error bar is visible. The TS value of this detection is just slightly above the threshhold 2 which results in a large error bar. Since the command replaces the spectral model of the source with a power law, this fit is not shown in Figures 6.5 and 6.6. Instead the cascade predictions created with CRPropa are shown for different magnetic fields in different colours since they have been used as the model during the analysis. In this Section the Gilmore EBL model was used during the simulations. The log likelihood values derived by `fit` during the analysis are included for each magnetic field strength in each time bin.

One can see the maximum flux of the prediction is higher for lower magnetic fields in all time bins. The difference between the maximum flux of the lowest and highest field strength decreases over time. The maximum flux of 10^{-20} G in the first time bin is around two orders of magnitude higher than the maximum flux of 10^{-16} G (see Figure 6.5a). At later time bins (see Figure 6.6c) the difference is around one order of magnitude. The time delay of the cascade photons depends on the strength of the IGMF (see Eq. (2.7)). For a higher magnetic field the time delay should increase meaning that in the late time bins the maximum flux should increase in comparsion to the lower magnetic fields.

Also the cascade maximum is at higher energies for higher magnetic field strength in all time bins. In the very late time bins (Figures 6.6c, 6.6d, 6.6e) it is also visible that the predictions are at lower energies than in the earlier time bins.

(a) SED for the 1st time bin.

(b) SED for the 2nd time bin.

(c) SED for the 3rd time bin.

(d) SED for the 4th time bin.

(e) SED for the 5th time bin.

(f) SED for the 6th time bin.

Figure 6.5: SEDs for 1st–6th time bin with Gilmore EBL model. The flux points of GRB221009A are shown in light blue. The cascade predictions for 10^{-20} G are shown in yellow, for $10^{-19.5}$ G in red, for 10^{-19} G in orange, for $10^{-18.5}$ G in green, for 10^{-18} G in dark blue, for $10^{-17.5}$ G in dark red, for 10^{-17} G in purple, for $10^{-16.5}$ G in turquoise and for 10^{-16} G in khaki.

Especially most of the simulations for 10^{-20} G are out of the chosen energy range of 100 MeV to 1 TeV. The time delay depends on the energy of the cascade photon (see Eq. (2.7)). For a higher photon energy the electron that scattered a CMB photon also had a high energy (see Eq. (2.2)). Such an electron travelled a smaller flight path (see Eq. (2.4)) which results in a smaller time delay. So the cascade photons with a higher energy arrive earlier at the observer.

28

(a) SED for the 7th time bin.

(b) SED for the 8th time bin.

(c) SED for the 9th time bin.

(d) SED for the 10th time bin.
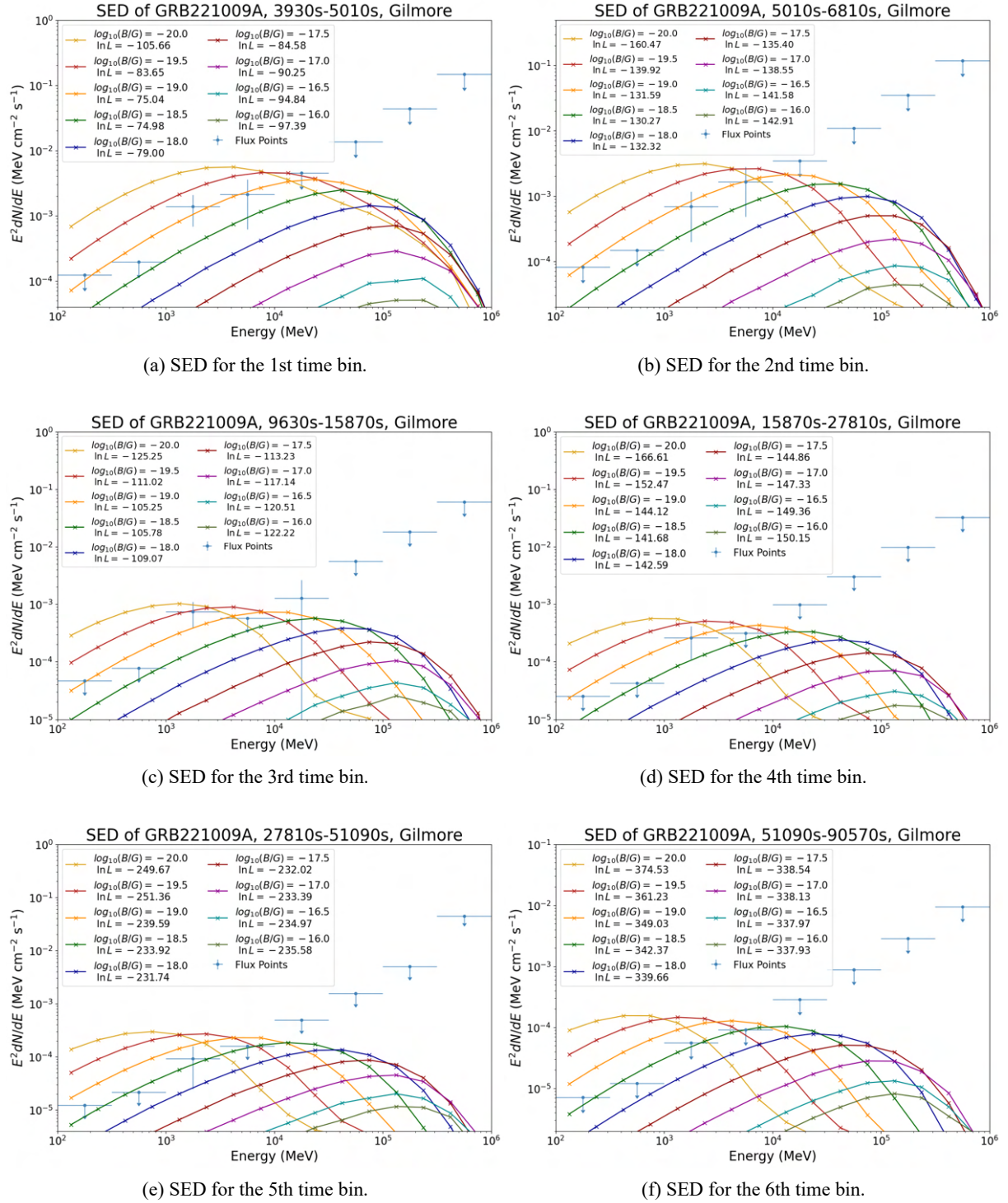
(e) SED for the 11th time bin.
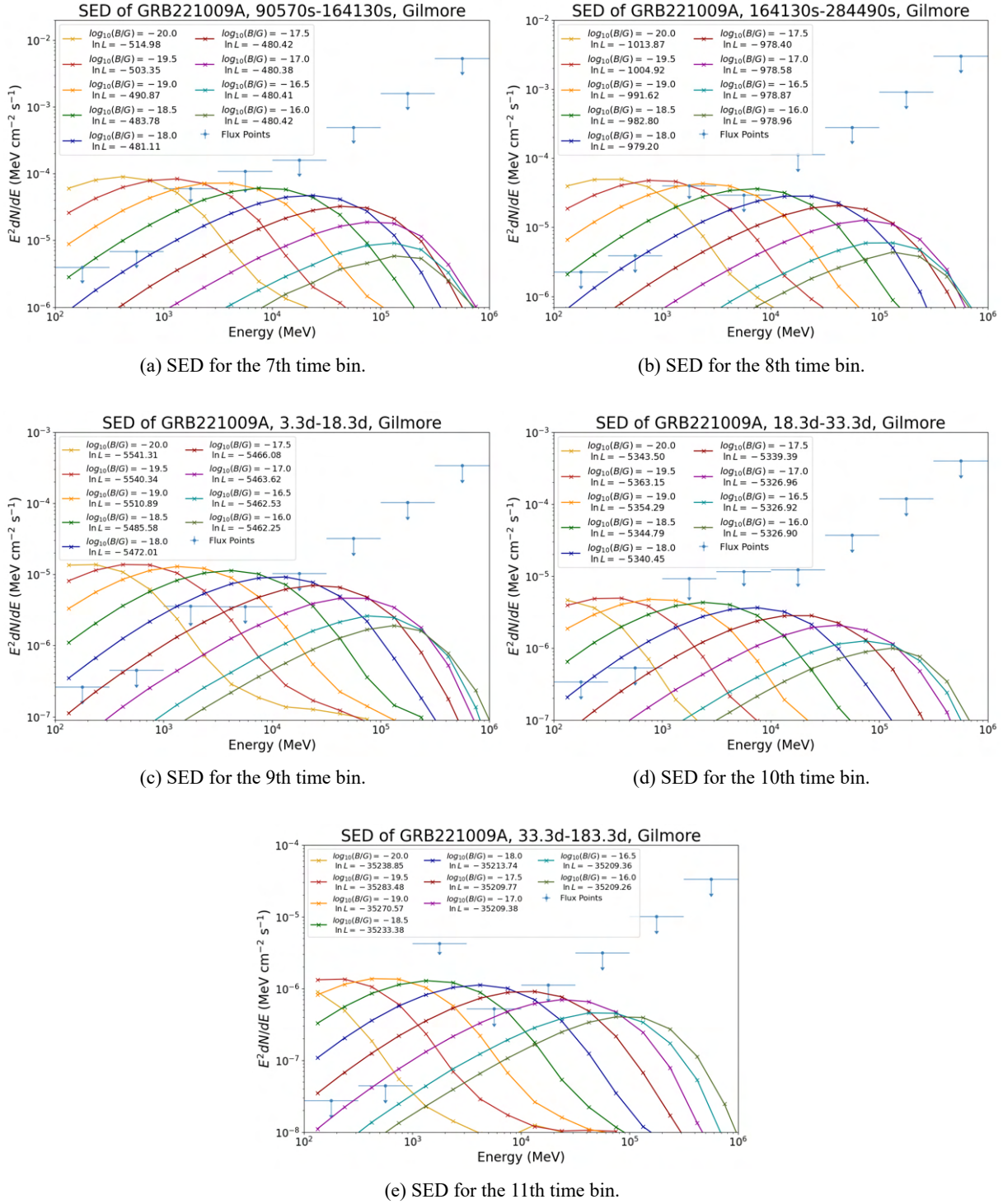
Figure 6.6: SEDs for 7th–11th time bin with Gilmore EBL model. The flux points of GRB221009A are shown in light blue. The cascade predictions for 10^{-20} G are shown in yellow, for $10^{-19.5}$ G in red, for 10^{-19} G in orange, for $10^{-18.5}$ G in green, for 10^{-18} G in dark blue, for $10^{-17.5}$ G in dark red, for 10^{-17} G in purple, for $10^{-16.5}$ G in turquoise and for 10^{-16} G in khaki.

6.2 Comparsion of EBL models

During their way through the universe VHE γ rays interact with the EBL (Section 2.1). For the EBL, different models exist which can be derived in three different ways (Section 2.1.1). All of the models have a different optical depth and intensity (see Figure 2.3). Due to that the

results may vary with different models. For this work the Gilmore [12], Franceschini [9] and the Finke [10] models were used and then compared, representing the three different approaches to derive EBL models mentioned in Section 2.1.1.

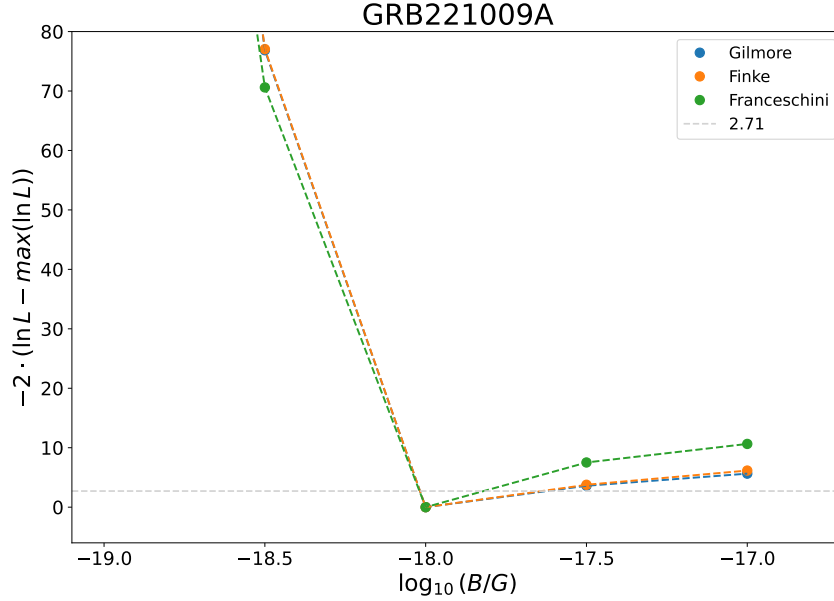Figure 6.7: Results of the log likehood ratio test for different EBL models. The result for Gilmore is shown in blue, the result for Finke in orange and for Franceschini in green. A linear interpolation was added for each result (shown as a dashed line).

The results for the three different models are shown in Figure 6.7. Gilmore in blue, Finke in orange and Franceschini in green. The exact values are shown in Table 6.4. For all three one can see a best fit at 10^{-18} G. That means that the IGMF has been detected if model explained in the beginning of Chapter 6 is correct. There is not a significant difference in the results for different EBL models. Due to that it is assumed that the choice of the EBL model does not make a difference in the following results. So only the Gilmore model is used in the following Section.

Table 6.4: Results of log likelihood ratio test for different EBL models.

B in G	Gilmore	Finke	Franceschini
10^{-20}	627.59	617.77	576.05
$10^{-19.5}$	548.02	543.11	513.05
10^{-19}	283.97	282.56	258.73
$10^{-18.5}$	76.86	77.05	70.61
10^{-18}	0.0	0.0	0.0
$10^{-17.5}$	3.60	3.77	7.52
10^{-17}	5.64	6.16	10.64

6.3 Including the Afterglow

So far any GRB afterglow emission was assumed to originate only from the cascade. But in early time bins also the astrophysical afterglow (Chapter 3) has to be taken into account. To

explain the afterglow, a second point-like source was added in the analysis in the first 8 time bins because the astrophysical afterglow is not expected to last longer. The spectrum of the afterglow is a priori not known. For the spectrum in the analysis, it was assumed to follow a power-law spectrum. Different indices ($\Gamma = 2$, 2.3, 2.5) were tested with the normalization free to vary. Also, two more magnetic field strengths were added ($10^{-16.5}$ and 10^{-16} G) than in Section 6.2.
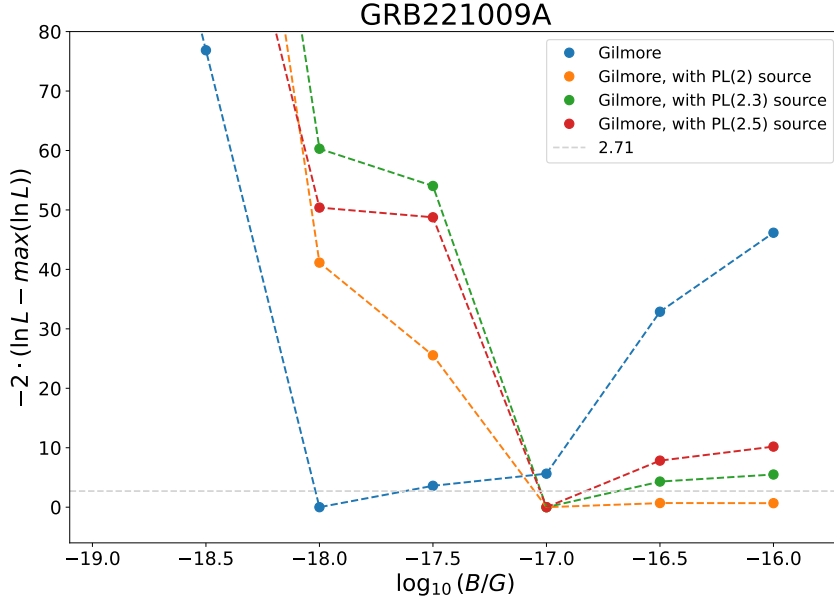

Figure 6.8: Results of the log likelihood ratio test with the Gilmore EBL model with and without different power law sources in the first 8 time bins. The result without the power law source is shown in blue, the result with a power law source with $\Gamma = 2$ in orange, with $\Gamma = 2.3$ in green and with $\Gamma = 2.5$ in red. A linear interpolation was added for each result (shown as a dashed line).

The results are shown in Figure 6.8 and Table 6.5. One can see the results without the afterglow model included in blue and with the different models in orange ($\Gamma = 2$), green ($\Gamma = 2.3$) and red ($\Gamma = 2.5$). The grey, dashed line is again at 2.71 (see Section 5.1). When the afterglow is included the results are changing. There is no longer a best fit at 10^{-18} G. The results with a power law source all have their minimum at 10^{-17} G. For $\Gamma = 2.3$ and 2.5 the results for $10^{-16.5}$ and 10^{-16} G are higher than 2.71. But for $\Gamma = 2$ the results are still below this value. As mentioned the spectrum of the afterglow is not known so it is not clear which results fit the spectrum the best. So one cannot speak about a best fit at 10^{-17} G. If $\Gamma > 2$, the assumed afterglow emission is too soft to explain the data. Then it is mostly explained with the cascade spectrum which has a hard spectrum ($\Gamma < 2$, see Figures 6.5 and 6.6).

Figure 6.9a shows the results without a power law source for each time bin. In Figure 6.9b it was zoomed in to lower values for the log likelihood ratio. The earlier time bins are shown in blue and the later time bins in red. The results for all time bins are shown in black (same as in Figure 6.8 in blue).

One can see for early time bins that the results are high for low magnetic fields (10^{-20} G) and high magnetic fields ($10^{-16.5}$ and 10^{-16} G). When looking at Figures 6.5a, 6.5b, 6.5c and 6.5d one can see that the predicted flux for 10^{-20} G is higher than the detections and upper limits

from the GRB at low energies. For high energies it is much lower than the measured GRB flux. The predicted flux for $10^{-16.5}$ and 10^{-16} G is very low at all energies, so it does not fit well, especially not for the energy ranges with a detection.

Table 6.5: Results of log likelihood ratio test with and without different power law sources.

B in G	without PL source	with PL(2) source	with PL(2.3) source	with PL(2.5) source
10^{-20}	627.59	703.68	687.05	714.20
$10^{-19.5}$	548.02	621.51	606.00	595.86
10^{-19}	283.97	373.74	356.35	346.03
$10^{-18.5}$	76.86	169.17	184.97	127.20
10^{-18}	0.0	41.14	60.29	50.40
$10^{-17.5}$	3.60	25.54	54.03	48.76
10^{-17}	5.64	0.0	0.0	0.0
$10^{-16.5}$	32.88	0.70	4.31	7.83
10^{-16}	46.16	0.68	5.50	10.19

For the last three time bins one can see very high values at $10^{-19.5}$ and 10^{-19} G with lower log likelihood ratio values at 10^{-20} G. When looking at Figures 6.6c, 6.6d and 6.6e we see that the maximum for the predicted flux of 10^{-20} G is at very low energies outside of the chosen energy range of $100\,\mathrm{MeV}$ and $1\,\mathrm{TeV}$. In that range most of the predicted flux is lower than the upper limits of the GRB. For $10^{-19.5}$ and 10^{-19} G on the other hand the maximum of the predicted flux is within the energy range and higher than the upper limits. The flux for $10^{-16.5}$ and 10^{-16} G is below all upper limits in those time bins which results in low log likelihood ratio values which one can see in Figure 6.9.

(a) Total range of the time resolved results.

(b) A zoom in to lower values of the log likelihood ratio up to 75.
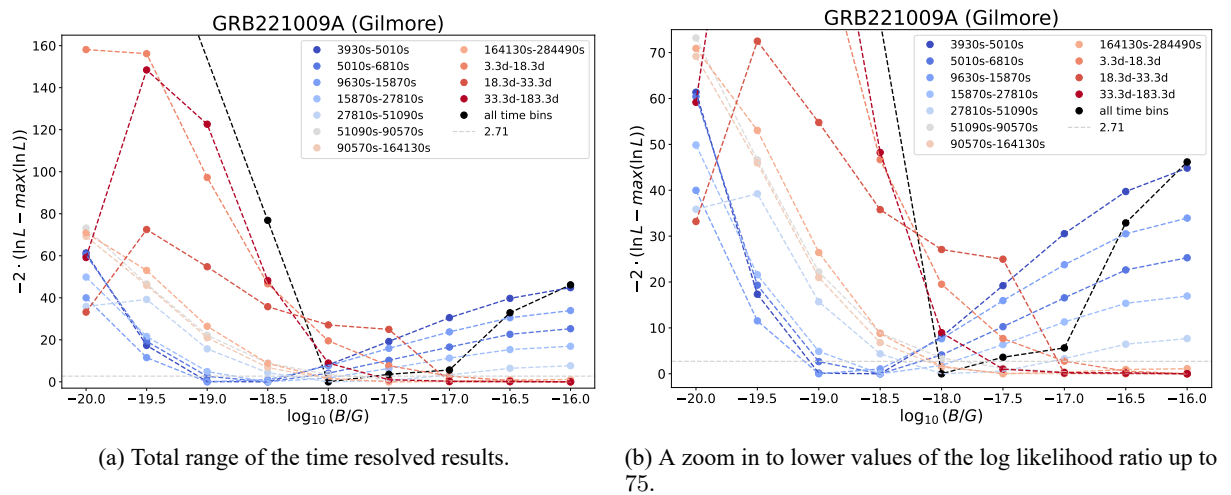
Figure 6.9: Time resolved results without a power law source. Early time bins are shown in blue and later time bins in red. All time bins are shown in black (same as in Figure 6.8 in blue).

Figure 6.10 shows the results for each time bin with a power law source. For each index the results are on the left side and a zoom into low log likelihood ratios on the right. The early time

bins are again shown in blue and the late time bins in red. The results for all time bins are shown in black (same as in Figure 6.8 in orange ($\Gamma = 2$), green ($\Gamma = 2.3$) and red ($\Gamma = 2.5$)). For all indices the results for the last three time bins are the same as in Figure 6.9 because in those time bins there were no power law source added as mentioned before.

(a) Total range of time resolved results with a power law source ($\Gamma = 2$).

(b) A zoom in to lower values of the log likelihood ratio up to 75 ($\Gamma = 2$).

(c) Total range of time resolved results with a power law source ($\Gamma = 2.3$).

(d) A zoom in to lower values of the log likelihood ratio up to 75 ($\Gamma = 2.3$).

(e) Total range of time resolved results with a power law source ($\Gamma = 2.5$).

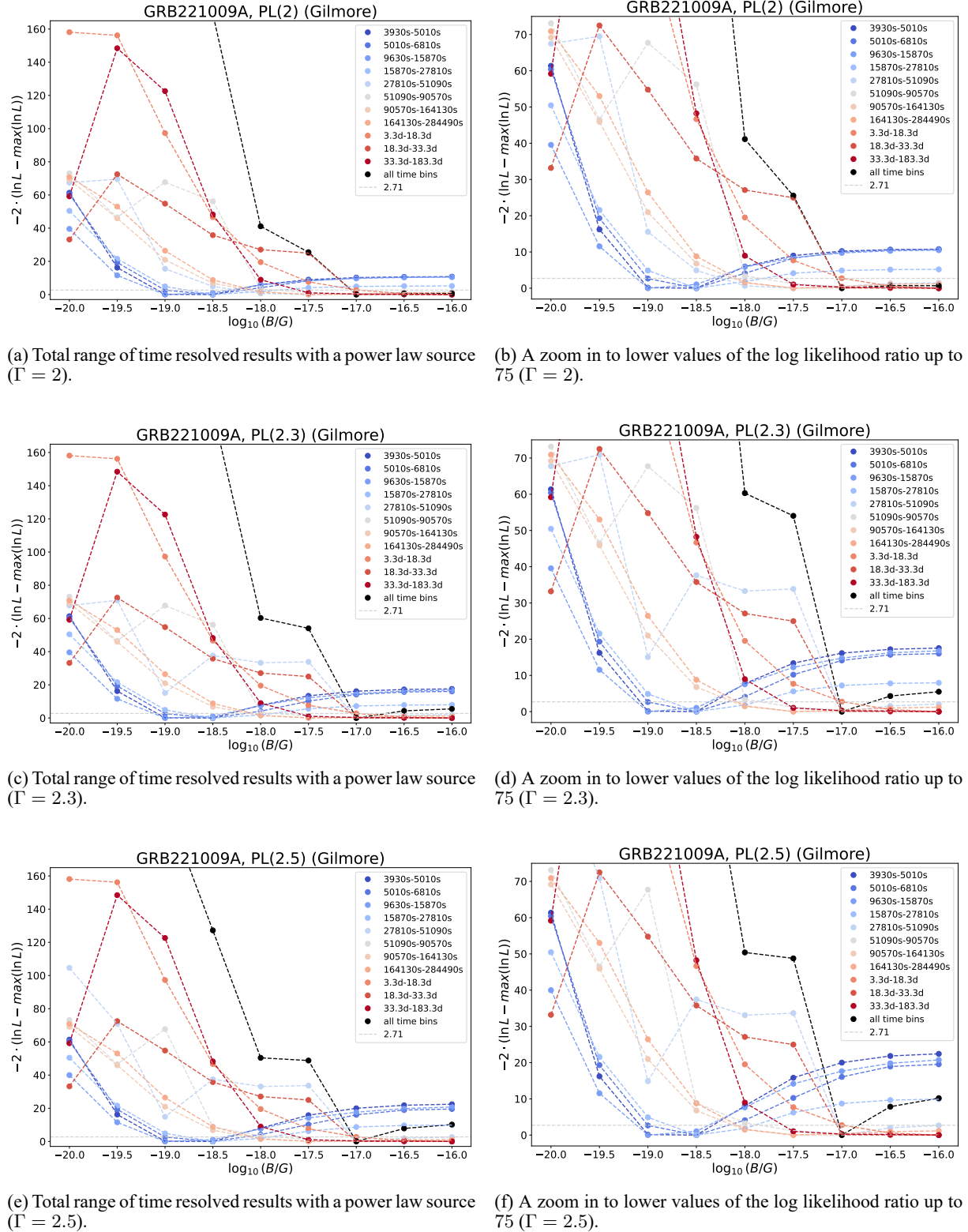(f) A zoom in to lower values of the log likelihood ratio up to 75 ($\Gamma = 2.5$).

Figure 6.10: Time resolved results with a power law source ($\Gamma = 2$, 2.3 and 2.5). Early time bins are shown in blue and later time bins in red. All time bins are shown in black (same as in Figure 6.8 in orange ($\Gamma = 2$), green ($\Gamma = 2.3$) and red ($\Gamma = 2.5$)).

Compared to Figure 6.9 in the early time bins the results are much lower at higher magnetic fields for all indices. They are the lowest for $\Gamma = 2$ (Figures 6.10a, 6.10b) and get higher with higher indices. A part of the detected flux of the GRB is now explained by the power law source which results in lower log likelihood ratio values for the higher magnetic fields since their predicted flux is below the upper limits in Figures 6.5a, 6.5b, 6.5c and 6.5d.

The shape of the results for time bins 5 and 6 changes with the power law source. One can see a drop at 10^{-19} G for $\Gamma = 2.3$ and 2.5 in the 5th time bin and another drop at $10^{-19.5}$ G in the 6th time bin for all indices. This might be due to an interplay between the power law source and the cascade. But in these time bins the power law sources are not significant which results in a bad fit and could explain the shape.

As mentioned before, CRPropa would probably not be sensitive to anything before $5,000$ s since the simulations predict a time delay for the primary photons within this time range (see Figure 6.1). This corresponds to the first two time bins (see Table 6.1). Because of that the first two time bins have been excluded from the results. This is shown in Figure 6.11 and Table 6.6.
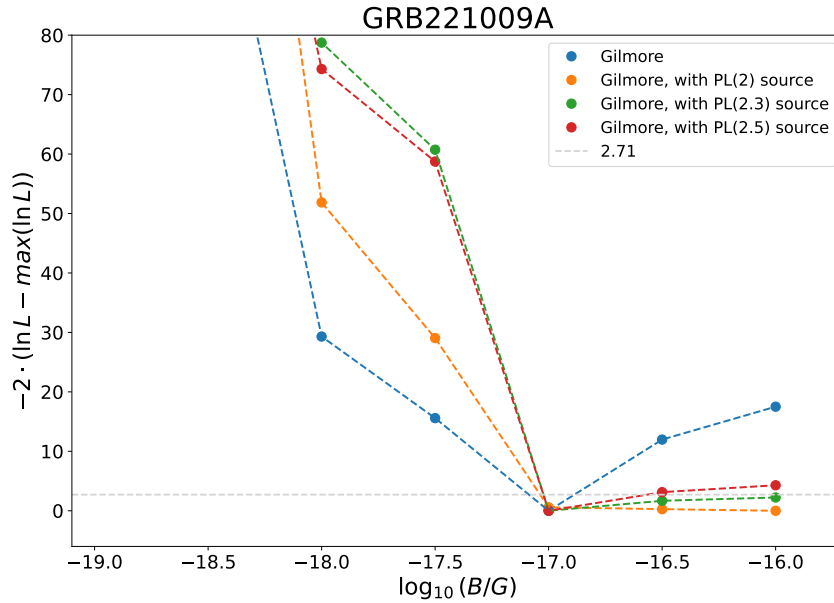

Figure 6.11: Results of the log likehood ratio test with the Gilmore EBL model with and without different power law sources without the first 2 time bins. The result without the power law source is shown in blue, the result with a power law source with $\Gamma = 2$ in orange, with $\Gamma = 2.3$ in green and with $\Gamma = 2.5$ in red. A linear interpolation was added for each result (shown as a dashed line).

One can see that the minimum without a power law source is now at 10^{-17} G instead of 10^{-18} G. Looking at Figure 6.9b this makes sense since those time bins have a big impact on the higher magnetic fields. Excluding them moves the minimum to a higher magnetic field. The results with a power law source with $\Gamma = 2.3$ and 2.5 still have the same structure with a minimum at 10^{-17} G but with higher values above 10^{-17} G. The values for 10^{-18} and $10^{-17.5}$ G are higher since the log likelihood ratio values in the first two time bins are low for these magnetic fields (see Fig. 6.10d, 6.10f). For $\Gamma = 2$ the minimum is now at 10^{-16} G and the log likelihood values for 10^{-17} and $10^{-16.5}$ G are just above 0. As one can see in Figure 6.10b all other time bins don't

have a big impact on 10^{-17}, $10^{-16.5}$ and 10^{-16} G. So it makes sense that these values are now even lower. From those results low magnetic fields below 10^{-17} G could be ruled out at $95\,\%$ confidence. As mentioned before the spectrum of the afterglow is not known. A fit of the data for the afterglow of [5] and using this model for the afterglow would improve the results.

Table 6.6: Results of loglikelihood ratio test with and without different power law sources excluding the dirst two time bins.

B in G	without PL source	with PL(2) source	with PL(2.3) source	with PL(2.5) source
10^{-20}	547.27	602.70	595.56	628.48
$10^{-19.5}$	552.82	606.77	600.75	596.38
10^{-19}	322.63	391.74	383.84	379.29
$10^{-18.5}$	118.31	189.95	215.25	163.25
10^{-18}	29.31	51.86	78.74	74.30
$10^{-17.5}$	15.58	29.05	60.73	58.74
10^{-17}	0.0	0.57	0.0	0.0
$10^{-16.5}$	11.97	0.26	1.68	3.13
10^{-16}	17.50	0.0	2.23	4.29

CHAPTER 7

Conclusion

The aim of this master thesis is to search for electron-positron pair cascades from GRB221009A. Cascade photons arrive at the observer with a time delay and can be used to constrain the IGMF. The cascade was simulated with CRPropa for magnetic field strengths between 10^{-20} and 10^{-16} G using the intrinsic spectrum obtained by LHAASO up to 13 TeV. This was used as a model for the analysis of the data from *Fermi*-LAT. For the analysis the python package *fermipy* was used. A log likelihood ratio test was performed to compare the models.

11 time bins were chosen for the analysis and the simulations. First the SEDs were generated for each time bin. It was shown that the maximum of the predicted flux is the highest for the lowest magnetic field. It was also shown that the maximum flux moves to lower energies in later times. This showed that the time delay depends on the magnetic field strength and the energy of the cascade photons. Then different models for the EBL were compared. VHE γ rays interact with the EBL during the production of the cascade. The simulations and analysis were done for the models by Gilmore [12], Finke [10] and Franceschini [9]. The results do not show any significant difference between the models. They all showed that a model with the cascade at $B = 10^{-18}$ G is preferred. The Gilmore model was then used for further analysis.

After that a second source with a power law spectrum was added in the analysis. Since the GRB was assumed to be just the cascade until that point this additional component should explain the astrophysical afterglow of the GRB. The spectrum of the afterglow is a priori unknown so different indices ($\Gamma = 2$, 2.3 and 2.5) for the power law were tested together with the cascade model. The results without the afterglow showed a best fit at 10^{-18} G. Including the afterglow the results showed a minimum at 10^{-17} G for all indices. It was also determined that CRPropa is not sensitive to the first two time bins at the chosen time resolution. They were excluded from the analysis. The results without the afterglow showed a best fit at 10^{-17} G. The results with the second source showed a minimum at 10^{-17} G for indices $\Gamma = 2.3$ and 2.5. For an index $\Gamma = 2$ a minimum at 10^{-16} G was found with values just above 0 for $10^{-16.5}$ G and 10^{-17} G.

From these results one can constrain the IGMF. Magnetic fields below 10^{-17} G can be ruled out at 95% confidence. But the spectrum of the afterglow of the burst is not known. A model of the afterglow data [5] would make the results more rebust against the choice of the spectral index.

7.1 Outlook

The next step is to derive predictions of the afterglow in the Fermi band. From [5] a model is currently being derived. This model will then be used for the analysis. Using this model could make the results more rebust against the choice of the spectral index. To get more precise limits, more simulations for magnetic field strengths between $10^{-17.5}$ and 10^{-17} should be done.
The predictions also depend on the model assumptions. In another study, a multi-messenger model for the prompt emission of the GRB within the intrnal shock scenario was used. Here, also photon indices of $\Gamma \leq 2$ for the spectrum, depending on the energy, were derived [38].

The detection of TeV γ rays from GRB221009A has important consequences for the search for physics beyond the Standard Model (SM). For example axions may effect the process of EBL absorption. Axions or axion-like-particles (ALPs) are hypothetical particles which are one of the most attractive candidates for cold dark matter. Their two photon coupling in external magnetic fields is the basis for their astrophysical detection. This process would lead to a suppression of the EBL absorption of high-energy γ rays [6].
Also leptonic models alone might not be sufficient to explain the afterglow emission of the burst above 10 TeV. This suggests the acceleration of ultrahigh-energy cosmic rays (UHECRs), which also can initiate electromagnetic cascades that contribute to the observed γ-ray flux [39]. UHECRs also get deflected by magnetic fields meaning the flux of the cascade depends on the magnetic fields along the line of sight. Further studies will investigate whether the cascade emission initiated by UHECRs can explain the GRB emission above 10 TeV [40].

Bibliography

[1] National Security Archive. URL: https://nsarchive.gwu.edu/briefing-book/nuclear-vault /2019-09-22/vela-flash-forty-years-ago, accessed: April 26, 2024.

[2] NASA, ESA and M. Kornmesser. URL: https://science.nasa.gov/missions/hubble/hubbl e-studies-gamma-ray-burst-with-highest-energy-ever-seen/, accessed: April 26, 2024.

[3] C. Grupen, *Astroparticle Physics*. Springer Cham, 2020.

[4] R. A. Batista and A. Saveliev, "The gamma-ray window to intergalactic magnetism," *Universe*, vol. 7, p. 223, jul 2021.

[5] L. Collaboration*† and et al., "A tera–electron volt afterglow from a narrow jet in an extremely bright gamma-ray burst," *Science*, vol. 380, no. 6652, pp. 1390–1396, 2023.

[6] "Very high-energy gamma-ray emission beyond 10 TeV from GRB 221009A," *Science Advances*, vol. 9, Nov. 2023.

[7] R. Plaga, "Detecting intergalactic magnetic fields using time delays in pulses of γ-rays," , vol. 374, pp. 430–432, Mar. 1995.

[8] E. Dwek and F. Krennrich, "The extragalactic background light and the gamma-ray opacity of the universe," *Astroparticle Physics*, vol. 43, p. 112–133, Mar. 2013.

[9] Franceschini, A., Rodighiero, G., and Vaccari, M., "Extragalactic optical-infrared background radiation, its time evolution and the cosmic photon-photon opacity ," *AA*, vol. 487, no. 3, pp. 837–852, 2008.

[10] J. D. Finke, S. Razzaque, and C. D. Dermer, "MODELING THE EXTRAGALACTIC BACKGROUND LIGHT FROM STARS AND DUST," *The Astrophysical Journal*, vol. 712, p. 238, feb 2010.

[11] G. Hinshaw, J. L. Weiland, R. S. Hill, N. Odegard, D. Larson, C. L. Bennett, J. Dunkley, B. Gold, M. R. Greason, N. Jarosik, E. Komatsu, M. R. Nolta, L. Page, D. N. Spergel, E. Wollack, M. Halpern, A. Kogut, M. Limon, S. S. Meyer, G. S. Tucker, and E. L. Wright,

"Five-Year Wilkinson Microwave Anisotropy Probe Observations: Data Processing, Sky Maps, and Basic Results," , vol. 180, pp. 225–245, Feb. 2009.

[12] R. C. Gilmore, R. S. Somerville, J. R. Primack, and A. Domínguez, "Semi-analytic modelling of the extragalactic background light and consequences for extragalactic gamma-ray spectra: Modelling of the EBL and gamma-ray spectra," *Monthly Notices of the Royal Astronomical Society*, vol. 422, p. 3189–3207, Apr. 2012.

[13] R. W. Klebesadel, I. B. Strong, and R. A. Olson, "Observations of Gamma-Ray Bursts of Cosmic Origin," , vol. 182, p. L85, June 1973.

[14] Swinburne University of Technology. *Gamma Ray Burst Types*. URL: https://astronomy. swin.edu.au/cosmos/G/gamma+ray+burst+types, accessed: April 24, 2024.

[15] P. Kumar and B. Zhang, "The physics of gamma-ray bursts & relativistic jets," *Physics Reports*, vol. 561, p. 1–109, Feb. 2015.

[16] G. Vedrenne and J.-L. Atteia, *Gamma-Ray Bursts, The brightest explosions in the Universe*. Springer Berlin, Heidelberg, 2009.

[17] NASA (2022). *NASA's Swift, Fermi Missions Detect Exceptional Cosmic Blast*. URL: https://www.nasa.gov/universe/nasas-swift-fermi-missions-detect-exceptional-cosmic-blast/, accessed: April 24, 2024.

[18] P. Veres, E. Burns, E. Bissaldi, S. Lesage, O. Roberts, and Fermi GBM Team, "GRB 221009A: Fermi GBM detection of an extraordinarily bright GRB," *GRB Coordinates Network*, vol. 32636, p. 1, Oct. 2022.

[19] E. Bissaldi, N. Omodei, M. Kerr, and Fermi-LAT Team, "GRB 221009A or Swift J1913.1+1946: Fermi-LAT detection," *GRB Coordinates Network*, vol. 32637, p. 1, Oct. 2022.

[20] S. Dichiara, J. D. Gropp, J. A. Kennea, N. P. M. Kuin, A. Y. Lien, F. E. Marshall, A. Tohuvavohu, M. A. Williams, and Neil Gehrels Swift Observatory Team, "Swift J1913.1+1946 a new bright hard X-ray and optical transient," *GRB Coordinates Network*, vol. 32632, p. 1, Oct. 2022.

[21] A. Saldana-Lopez, A. Domínguez, P. G. Pérez-González, J. Finke, M. Ajello, J. R. Primack, V. S. Paliya, and A. Desai, "An observational determination of the evolving extragalactic background light from the multiwavelength HST/CANDELS survey in the Fermi and CTA era," *Monthly Notices of the Royal Astronomical Society*, vol. 507, p. 5144–5160, Aug. 2021.

[22] F. Aharonian and et al, "Constraints on the Intergalactic Magnetic Field Using Fermi-LAT and H.E.S.S. Blazar Observations," *The Astrophysical Journal Letters*, vol. 950, p. L16, June 2023.

[23] Y.-Y. Huang, C.-Y. Dai, H.-M. Zhang, R.-Y. Liu, and X.-Y. Wang, "Constraints on the Intergalactic Magnetic Field Strength from γ-Ray Observations of GRB 221009A," , vol. 955, p. L10, Sept. 2023.

[24] I. Vovk, A. Korochkin, A. Neronov, and D. Semikoz, "Constraints on the intergalactic magnetic field from Fermi/LAT observations of the 'pair echo' of GRB 221009A," , vol. 683, p. A25, Mar. 2024.

[25] NASA. URL: https://en.wikipedia.org/wiki/Fermi_Gamma-ray_Space_Telescope#/media/File:Fermi_Gamma-ray_Space_Telescope_spacecraft_model.png, accessed: March 15, 2024.

[26] W. B. Atwood and et al., "THE LARGE AREA TELESCOPE ON THE FERMI GAMMA-RAY SPACE TELESCOPEMISSION," *The Astrophysical Journal*, vol. 697, p. 1071–1102, May 2009.

[27] NASA (Nov. 2022). *Fermitools: Cicerone*. URL: https://fermi.gsfc.nasa.gov/ssc/data/analysis/documentation/Cicerone/, accessed: April 9, 2024.

[28] R. L. Workman and Others, "Review of Particle Physics," *PTEP*, vol. 2022, p. 083C01, 2022.

[29] W. A. Rolke, A. M. López, and J. Conrad, "Limits and confidence intervals in the presence of nuisance parameters," *Nuclear Instruments and Methods in Physics Research Section A: Accelerators, Spectrometers, Detectors and Associated Equipment*, vol. 551, p. 493–503, Oct. 2005.

[30] P. Lipari, "The origin of the power–law form of the extragalactic gamma–ray flux," *Astroparticle Physics*, vol. 125, p. 102507, Feb. 2021.

[31] M. Wood, R. Caputo, E. Charles, M. D. Mauro, J. Magill, and J. Perkins, "Fermipy: An open-source Python package for analysis of Fermi-LAT Data," 2017.

[32] Fermipy Developers (2016-2024). *Fermipy Documentation*. URL: https://fermipy.readthedocs.io/en/latest/index.html, accessed: April 12, 2024.

[33] R. A. Batista, J. B. Tjus, J. Dörner, A. Dundovic, B. Eichmann, A. Frie, C. Heiter, M. R. Hoerbe, K.-H. Kampert, L. Merten, G. Müller, P. Reichherzer, A. Saveliev, L. Schlegel, G. Sigl, A. van Vliet, and T. Winchen, "CRPropa 3.2 — an advanced framework for high-energy particle propagation in extragalactic and galactic spaces," *Journal of Cosmology and Astroparticle Physics*, vol. 2022, p. 035, sep 2022.

[34] CRPropa Developers (2024). *CRPropa*. URL: https://crpropa.github.io/CRPropa3/index.html, accessed: April 15, 2024.

[35] M. Settimo and M. De Domenico, "Propagation of extragalactic photons at ultra-high energy with the EleCa code," *Astroparticle Physics*, vol. 62, p. 92–99, Mar. 2015.

[36] S. Lee, "Propagation of extragalactic high energy cosmic and γ rays," *Physical Review D*, vol. 58, July 1998.

[37] Fermi/LAT Collaboration, "GRB 221009A: the B.O.A.T. Burst that Shines in Gamma-rays," In preperation.

[38] A. Rudolph, M. Petropoulou, W. Winter, and Ž. Bošnjak, "Multi-messenger Model for the Prompt Emission from GRB 221009A," , vol. 944, p. L34, Feb. 2023.

[39] S. Das and S. Razzaque, "Ultrahigh-energy cosmic-ray signature in GRB 221009A," *Astronomy & Astrophysics*, vol. 670, p. L12, Feb. 2023.

[40] J. Müller, "Investigating the origin of multi TeV emission of the GRB 221009A," Master's thesis, University of Southern Denmark, expected 2024. In preperation.

[41] A. Baktash, D. Horns, and M. Meyer, "Interpretation of multi-TeV photons from GRB221009A," 2023.

APPENDIX A

Appendix

A.1   Configuration files for *fermipy* and CRPropa

```
data:
  evfile : data.txt
  scfile : L23053107163761B555A348_SC00.fits
  ltcube: null

binning:
  roiwidth   : 10.0
  binsz      : 0.1
  binsperdec : 8
  proj: CAR

selection :
  emin : 100 #MeV
  emax : 1000000 #MeV
  zmax    : 90 #deg
  evclass : 128
  evtype  : 3
  ra : 288.21
  dec : 19.73
  tmin    : 687018154.988  # 2022-10-09 14:22:29.988 UTC
  tmax    : 687019234.988  # 2022-10-09 14:40:29.988 UTC
  filter  : 'DATA_QUAL>0 && LAT_CONFIG==1'

gtlike:
  edisp : True
  irfs : 'P8R3_SOURCE_V3'
  edisp_disable : ['isodiff']

model:
  src_roiwidth : 15.0
  galdiff  : 'gll_iem_v07.fits'
  isodiff  : 'iso_P8R3_SOURCE_V3_v1.txt'
  catalogs : ['gll_psc_v30.fit']
  sources  :
    - Normalization: 1
      SpatialModel: PointSource
      SpectrumType: FileFunction
      Spectrum_Filename: 'energies_B16.0_tb1.txt'
      ra: 288.21
      dec: 19.73
      name: GRB221009A
```

Figure A.1: Configuration file for the *fermipy* analysis of the 1st time bin and $B = 10^{-16}$ G. The file includes all settings made for the analysis. The period of time was changed for each time bin and the spectrum for each magnetic field and time bin.

```
Simulation:
    multiplicity: 40
    Nbatch: [100, 100, 100, 100, 100, 100, 100, 100, 100, 100, 100,
             100, 100, 100, 100, 100, 100, 100, 100, 100, 100, 100,
             100, 100, 100, 100, 100, 100, 100, 100, 100, 100, 100,
             100, 100, 100, 100, 100, 100, 100, 100, 100, 100, 100,
             100]
    emcasc: True # if false, only calculate neutrinos
    maxStepLength: 0.5 # in Mpc
    tol: 1.e-16
    minTresol: "2 min"
    include_CMB: True
    include_z_evol: True
    include_higher_order_pp: False
    thinning: 0.
    propagation: "CK"  # BP or CK
    name: ""
    outputtype: 'ascii'  # ascii or hdf5
    forward_approx: True

Cosmology:
    Om: 0.3
    h: 0.7

Source:
    Composition: 22
    z: 0.1505 # source redshift, source position is at (D,0,0)
    th_jet: 1.6 # jet opening angle in degrees, emission in -x
direction - don't go below 0.1 degree
    Emin: [1.00000000e+09, 1.25892541e+09, 1.58489319e+09,
1.99526231e+09,
           2.51188643e+09, 3.16227766e+09, 3.98107171e+09,
5.01187234e+09,
           6.30957344e+09, 7.94328235e+09, 1.00000000e+10,
1.25892541e+10,
           1.58489319e+10, 1.99526231e+10, 2.51188643e+10,
3.16227766e+10,
           3.98107171e+10, 5.01187234e+10, 6.30957344e+10,
7.94328235e+10,
           1.00000000e+11, 1.25892541e+11, 1.58489319e+11,
1.99526231e+11,
           2.51188643e+11, 3.16227766e+11, 3.98107171e+11,
5.01187234e+11,
           6.30957344e+11, 7.94328235e+11, 1.00000000e+12,
1.25892541e+12,
           1.58489319e+12, 1.99526231e+12, 2.51188643e+12,
3.16227766e+12,
           3.98107171e+12, 5.01187234e+12, 6.30957344e+12,
7.94328235e+12,
           1.00000000e+13, 1.25892541e+13, 1.58489319e+13,
1.99526231e+13,
           2.51188643e+13]
    Emax: [1.25892541e+09, 1.58489319e+09, 1.99526231e+09,
2.51188643e+09,
```

Figure A.2: First part of a configuration file for the CRPropa simulations $B = 10^{-16.5}$ G. The file includes all settings made for the simulations. The magnetic field strength was changed for each B-field tested. The file is continued in Fig. A.3.

```
            3.16227766e+09, 3.98107171e+09, 5.01187234e+09,
6.30957344e+09,
            7.94328235e+09, 1.00000000e+10, 1.25892541e+10,
1.58489319e+10,
            1.99526231e+10, 2.51188643e+10, 3.16227766e+10,
3.98107171e+10,
            5.01187234e+10, 6.30957344e+10, 7.94328235e+10,
1.00000000e+11,
            1.25892541e+11, 1.58489319e+11, 1.99526231e+11,
2.51188643e+11,
            3.16227766e+11, 3.98107171e+11, 5.01187234e+11,
6.30957344e+11,
            7.94328235e+11, 1.00000000e+12, 1.25892541e+12,
1.58489319e+12,
            1.99526231e+12, 2.51188643e+12, 3.16227766e+12,
3.98107171e+12,
            5.01187234e+12, 6.30957344e+12, 7.94328235e+12,
1.00000000e+13,
            1.25892541e+13, 1.58489319e+13, 1.99526231e+13,
2.51188643e+13,
            3.16227766e+13]
    useSpectrum: False # if True, simulate spectrum, otherwise
inject delta function with energy E
    source_morphology: cone
    #source_morphology: dir

Observer:
    obsPosX: 0. # observer's x coordinate
    obsPosY: 0. # observer's y coordinate
    obsPosZ: 0. # observer's z coordinate
    obsAngle: 0. # angle w.r.t. to jet axis, if non-zero, overwrites
source position
    zmin: null
    obsSmallSphere: False

BreakConditions:
    Dmax: 0.624131779348077 # maximum distance of particle for
tracing in Gpc
    Emin: 1.e+8 # minimum energy for particle tracing
    minRigidity: 50.

Bfield:
    type: turbulence # either cell or turbulence
    B: [3.162278e-17] # rms of B field in Gauss
    seed: 2308 # random seed for B field
    NBgrid: 100 # number of B-field cells
    boxSize: 50 # box size for vector grid in Mpc
    maxTurbScale: 25. # maximum turbulence scale in Mpc
    turbIndex: -1.667 # turbulence index, default - 11/3
    periodicity: 4000. # length of periodic box in Mpc
    EBL: IRB_Gilmore12
```

Figure A.3: Second part of a configuration file for the CRPropa simulations $B = 10^{-16.5}$ G. The file includes all settings made for the simulations. The magnetic field strength was changed for each B-field tested.

A.2 Log likelihood ratio test using SEDs

In preperation two methods of deriving the log likelihood values were compared. In Chapter 6 the method `fit` was used. The log likelihood values were also derived using the `sed` method. One can find an explaination of this method and a comparsion in this section. Due to the missing data from [6] the spectral parameters for the simulations were derived from [41]. It was assumed to be described by a log parabola with an exponential cutoff at $13\,\mathrm{TeV}$ (see eq. (5.11)). The exact parameter choices are shown in Table A.1. Magnetic fields from $B = 10^{-19}$ to $10^{-17}\,\mathrm{G}$ were tested.

Table A.1: Parameters for the spectral shape of the cascade used for the simulations.

Parameter	Selection
Prefactor	$1.561 \cdot 10^{-19} \frac{1}{(cm^2\,eV\,s)}$
Scale	$10^{12}\,\mathrm{eV}$
Index	2.296
Cutoff	$1.3 \cdot 10^{13}\,\mathrm{eV}$

For the comparsion only time bins 3 - 11 from Table 6.1 were used. The parameter choices for the analysis using *fermipy* are shown in Table A.2. An energy range from $1\,\mathrm{GeV}$ to $1\,\mathrm{TeV}$ was chosen. A maximum zenith angle of $105°$ was used to reduce the contamination from the γ-rays Earth limb. All other parameters are the same as in Chapter 6. Figures A.4 and A.5 show the measured flux for each used time bin generated by `sed` during the analysis in blue. The cascade predictions created with CRPropa are shown for different magnetic fields in different colours. The log likelihood values derived by `fit` during the analysis using the simulations as a file function model for the GRB are included for each B field in each time bin.

Table A.2: Parameters the analysis using *fermipy*.

Parameter	Selection
Time Range	6 months
Energy Range	$>1\,\mathrm{GeV}$
ROI size	$10° \times 10°$
Max. Zenith Angle	$105°$
Filter	`DATA_QUAL>0 && LAT_CONFIG==1`
Spatial binning	$0.1°$ / pixel
Energy binning	8 bins per decade
Event Class / IRFs	`P8R3_SOURCE_V3`

(a) SED for the 1st time bin.

(b) SED for the 2nd time bin.

(c) SED for the 3rd time bin.

(d) SED for the 4th time bin.

(e) SED for the 5th time bin.
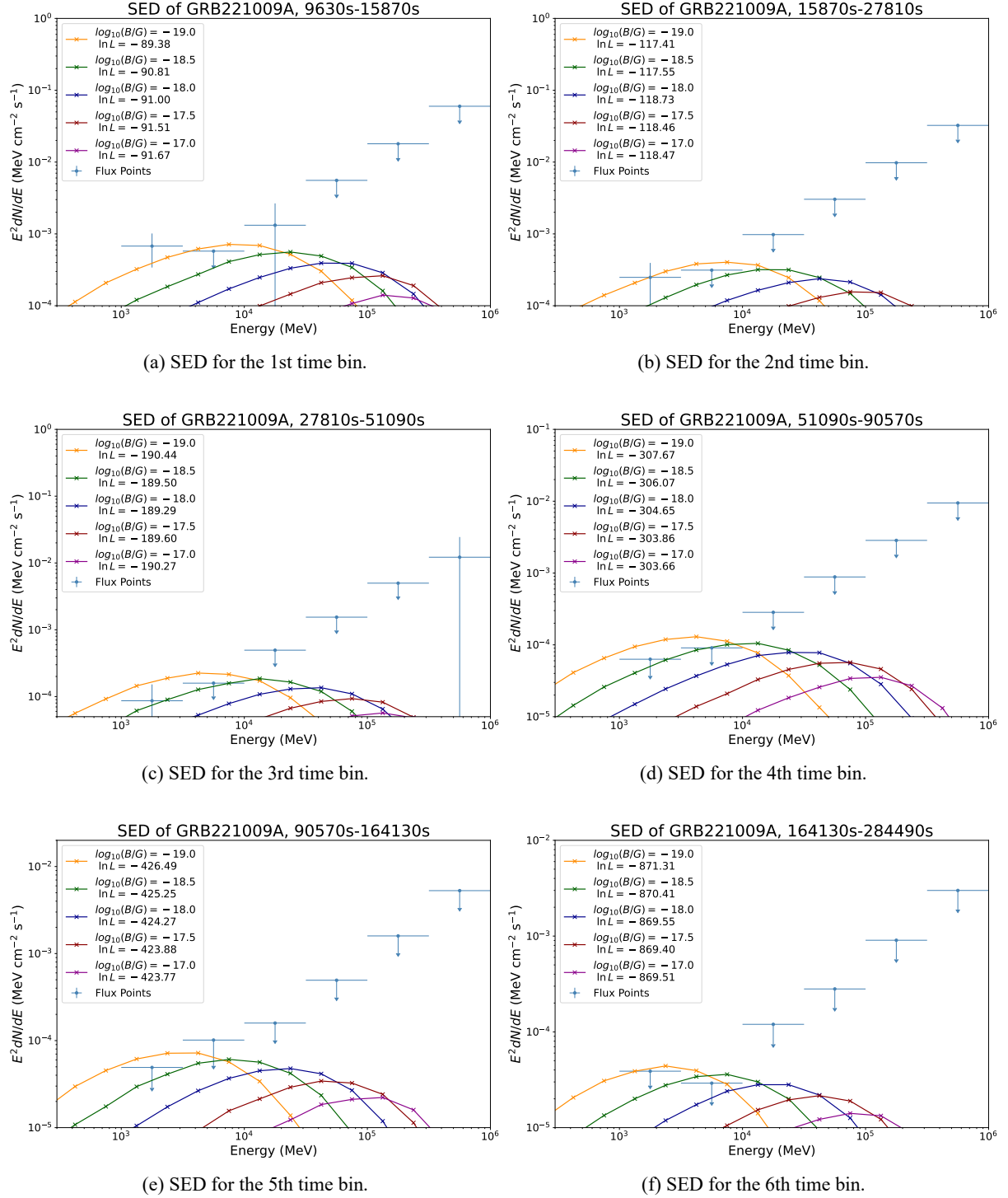
(f) SED for the 6th time bin.

Figure A.4: SEDs for 1st–6th time bin with Gilmore EBL model. The flux points of GRB221009A are shown in light blue. The cascade predictions for 10^{-19} G are shown in orange, for $10^{-18.5}$ G in green, for 10^{-18} G in dark blue, for $10^{-17.5}$ G in dark red and for 10^{-17} G in purple.

(a) SED for the 7th time bin.

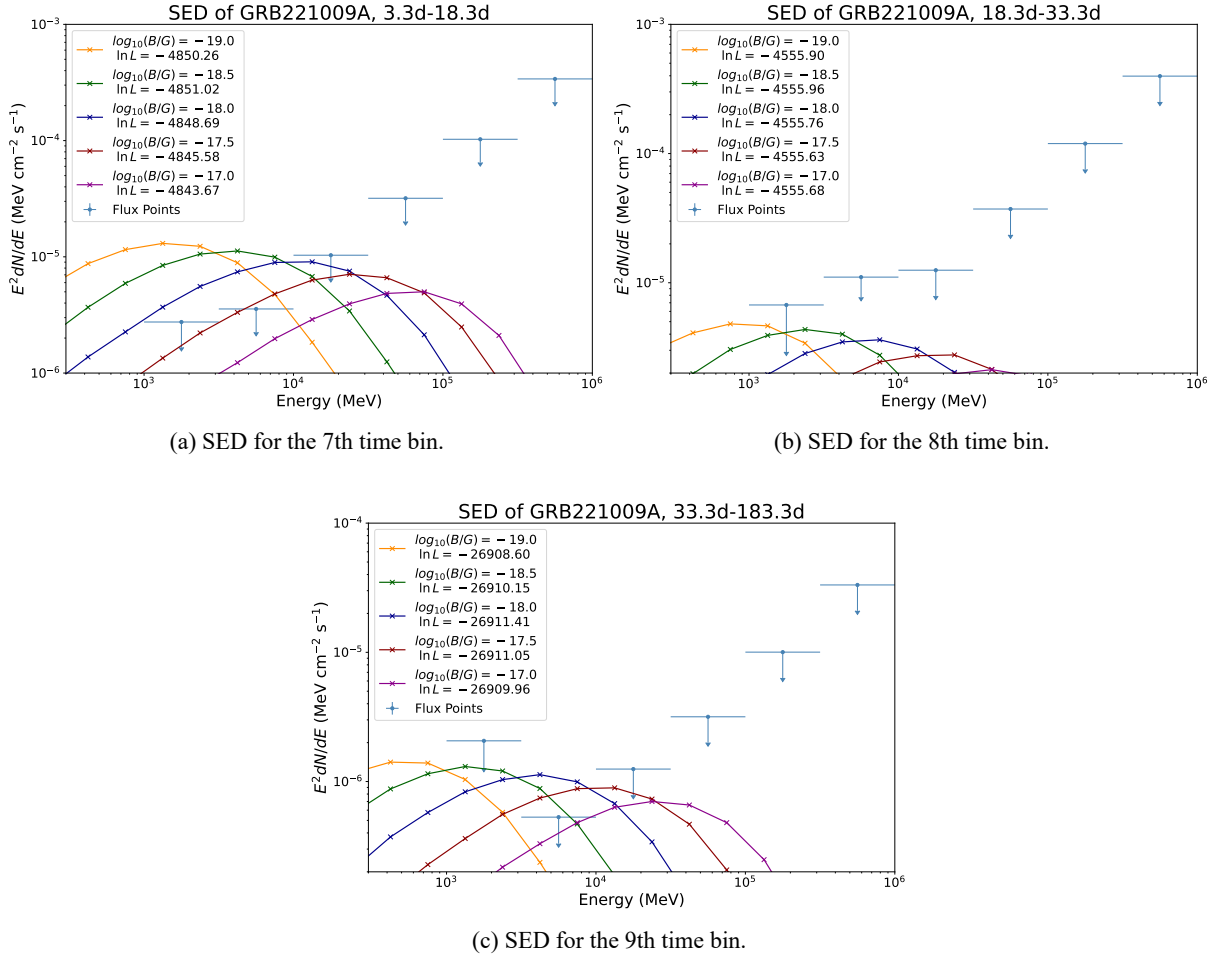(b) SED for the 8th time bin.

(c) SED for the 9th time bin.

Figure A.5: SEDs for 5th–9th time bin with Gilmore EBL model. The flux points of GRB221009A are shown in light blue. The cascade predictions for 10^{-19} G are shown in orange, for $10^{-18.5}$ G in green, for 10^{-18} G in dark blue, for $10^{-17.5}$ G in dark red and for 10^{-17} G in purple.

For the `sed` method the simulations were not used during the analysis. Instead the spectrum of the GRB was assumed to be described by a log parabola point source (see eq. (5.9)). When computing the SEDs the log likelihood values are given for the flux in each energy bin. This is shown in Figure 5.1 for the first time bin. An interpolation of the energy flux over the log likelihood values has been done for each energy bin. This is shown in Figure A.6 for the first two energy bins in the first time bin. The energy flux value of the cascade for different magnetic fields in each energy bin were simulated by CRPropa. The log likelihood values for each predicted energy flux were taken from the interpolation. This has been done for each time bin. The log likelihood values were then sumed up over energy and time. Afterwards the log likehood ratio was calculated (eq. (5.7)). As mentioned before the log likelihood values were also derived using `fit` as in Chapter 6. Those were also summed up over time for each magnetic field and the log likehood ratio was calculated.

Figure A.7 shows the results of log likelihood ratio test. In blue one can see the result for the `sed` method with a linear interpolation for visualisation. The result using the simulations as a file function and deriving the log likelihood with `fit` is shown in orange labelled "with file function model". Here one can see a best fit at $10^{-17.5}$ G.

(a) Interpolation first energy bin
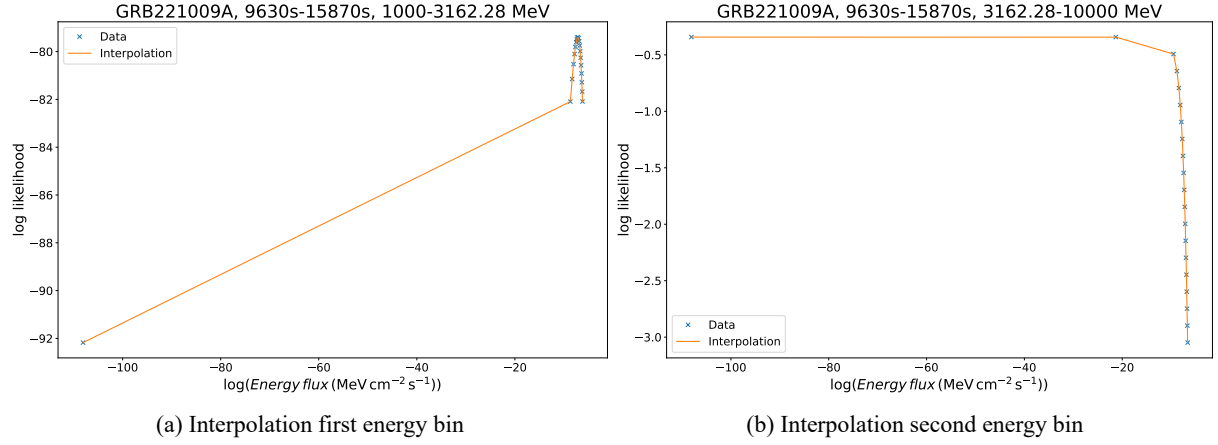
(b) Interpolation second energy bin

Figure A.6: Interpolation of the energy flux over the log likelihood values for the first two energy bins in the first time bin. The data from the analysis is shown as blue crosses and the linear interpolation in orange.

From the `sed` method one could rule out low magnetic fields at $95\,\%$ confidence. The exact values are shown in Table A.3. It also seems like the SED method is more constraining than the file function method. Due to that it is assumed than the file function method is more accurate. That's why for the following analysis only the file function method is used.
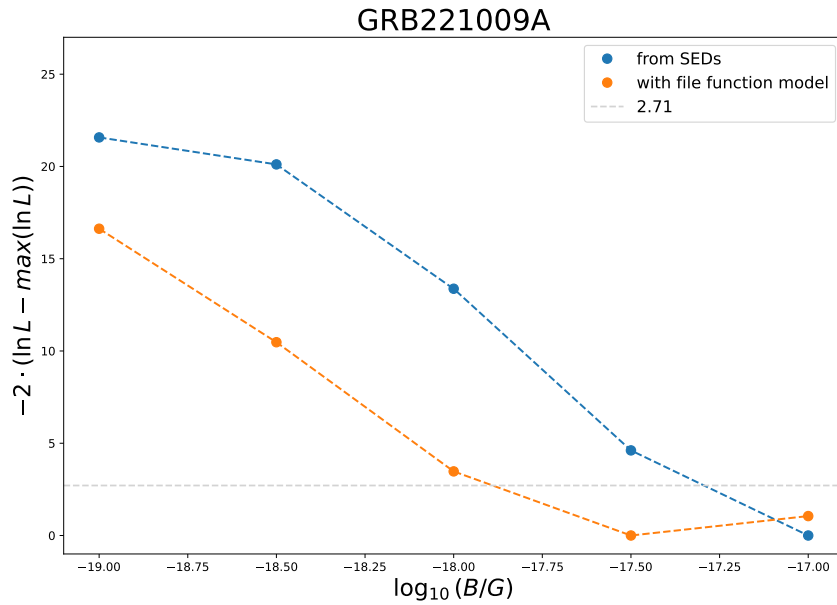

Figure A.7: Results of the log likehood ratio test for different EBL models. The result for the `sed` method is shown in blue and the result using a file function and the method `fit` is shown in orange. A linear interpolation was added for each result (shown as a dashed line).

Table A.3: Results of the log likelihood ratio test for different methods.

B in G	`sed` method	file function (`fit`) method
10^{-19}	21.57	16.63
$10^{-18.5}$	20.11	10.47
10^{-18}	13.37	3.47
$10^{-17.5}$	4.61	0.0
10^{-17}	0.0	1.05

Acknowledgements

Firstly, I want to thank Manuel Meyer for giving me the opportunity to work on this project and for providing guidance and feedback. You've been a great supervisor.

A special thank you to everyone from the Axion-ALP-DM research group in Hamburg and at SDU: Rahul Cecil, Sara Porras Bedmar, Gulden Othman, Atreya Acharyya, Johanna Müller, Eike Ravensburg, Elmeri Rivasto and Nelson Nelle, thank you for being a great bunch of people. Thank you for the support, friendship and distraction (when needed). It's been great fun working with you all! Rahul and Atreya in particular thanks for proofreading this thesis.

I am grateful to everyone I've collaborated with externally: Paolo Da Vela, Guillem Martí-Devesa, Francesco Saturni, Antonio Stamerra, Peter Veres and Francesco Longo, thank you all for your support and input.

Finally, but the most importantly, I would like to thank my family and friends for their support during the last year.

Eidesstattliche Erklärung

Ich versichere, dass ich die beigefügte schriftliche Masterarbeit selbstständig angefertigt und keine anderen als die angegebenen Hilfsmittel benutzt habe. Alle Stellen, die dem Wortlaut oder dem Sinn nach anderen Werken als der oben genannten Publikation entnommen sind, habe ich in jedem einzelnen Fall unter genauer Angabe der Quelle deutlich als Entlehnung kenntlich gemacht. Dies gilt auch für alle Informationen, die dem Internet oder anderer elektronischer Datensammlungen entnommen wurden.

Ich erkläre ferner, dass die von mir angefertigte Masterarbeit in gleicher oder ähnlicher Fassung noch nicht Bestandteil einer Studien- oder Prüfungsleistung im Rahmen meines Studiums war.

Ich bin damit einverstanden, dass die Masterarbeit veröffentlicht wird.

Hamburg, 19.05.24

Ort, Datum   Unterschrift